THE UNIVERSITY of EDINBURGH

Edinburgh Research Explorer

Collective magnetotaxis of microbial holobionts is optimized by the three-dimensional organization and magnetic properties of ectosymbionts

Citation for published version:
Chevrier, DM, Juhin, A, Menguy, N, Bolzoni, R, Soto-Rodriguez, PED, Kojadinovic-Sirinelli, M, Paterson, GA, Belkhou, R, Williams, W, Skouri-Panet, F, Kosta, A, Le guenno, H, Pereiro, E, Faivre, D, Benzerara, K, Monteil, CL & Lefevre, CT 2023, 'Collective magnetotaxis of microbial holobionts is optimized by the three-dimensional organization and magnetic properties of ectosymbionts', *Proceedings of the National Academy of Sciences (PNAS)*, vol. 120, no. 10, e2216975120. https://doi.org/10.1073/pnas.2216975120

Digital Object Identifier (DOI):
10.1073/pnas.2216975120

Link:
Link to publication record in Edinburgh Research Explorer

Document Version:
Peer reviewed version

Published In:
Proceedings of the National Academy of Sciences (PNAS)

General rights
Copyright for the publications made accessible via the Edinburgh Research Explorer is retained by the author(s) and / or other copyright owners and it is a condition of accessing these publications that users recognise and abide by the legal requirements associated with these rights.

Take down policy
The University of Edinburgh has made every reasonable effort to ensure that Edinburgh Research Explorer content complies with UK legislation. If you believe that the public display of this file breaches copyright please contact openaccess@ed.ac.uk providing details, and we will remove access to the work immediately and investigate your claim.

Download date: 02. Mar. 2023

Collective magnetotaxis of microbial holobionts is optimized by the three-dimensional organization and magnetic properties of ectosymbionts

Daniel M. Chevrier[1*], Amélie Juhin[2], Nicolas Menguy[2], Romain Bolzoni[1], Paul E. D. Soto-Rodriguez[1], Mila Kojadinovic-Sirinelli[1], Greig A. Paterson[3], Rachid Belkhou[4], Wyn Williams[5], Fériel Skouri-Panet[2], Artemis Kosta[6], Hugo Le Guenno[6], Eva Pereiro[7], Damien Faivre[1], Karim Benzerara[2], Caroline L. Monteil[1], Christopher T. Lefevre[1*]

[1]Aix-Marseille Université, CNRS, CEA, UMR7265, BIAM, Saint-Paul-lez-Durance 13108, France

[2]Sorbonne Université, UMR CNRS 7590, MNHN, IRD, Institut de Minéralogie, de Physique des Matériaux et de Cosmochimie, IMPMC, 75005, Paris, France

[3]Department of Earth, Ocean and Ecological Sciences, University of Liverpool, L69 7ZE, Liverpool, UK

[4]Synchrotron Soleil, L'Orme des Merisiers, Saint-Aubin -BP 48, 91192 Gif-sur-Yvette Cedex, France

[5]University of Edinburgh, School of GeoSciences, Grant Institute, West Mains Road, Edinburgh EH9 3JW

[6]Plateforme de Microscopie de l'Institut de Microbiologie de la Méditerranée, IMM, Institut de Microbiologie, FR3479, Campus CNRS, 13402 Marseille cedex 20, France

[7]ALBA Synchrotron Light Source, Cerdanyola del Vallés, Barcelona 08290, Spain

***Corresponding authors**: Drs. Daniel Chevrier and Christopher T. Lefevre

Emails: daniel.chevrier@cea.fr and christopher.lefevre@cea.fr

ORCID: Daniel M. Chevrier (0000-0002-0914-6714), Amélie Juhin (0000-0003-0752-3034), Nicolas Menguy (0000-0003-4613-2490), Romain Bolzoni (0000-0002-5741-3856), Paul E. D. Soto-Rodriguez (0000-0002-2425-932X), Mila Kojadinovic-Sirinelli (0000-0001-8110-3113), Greig A. Paterson (0000-0002-6864-7420), Rachid Belkhou (0000-0002-2218-7481), Wyn Williams (0000-0001-9210-7574), Fériel Skouri-Panet (0000-0002-2623-9058), Artemis Kosta (0000-0001-7115-4566), Hugo Le Guenno (0000-0003-1768-1212), Eva Pereiro (0000-0001-7626-5935), Damien Faivre (0000-0001-6191-3389), Karim Benzerara (0000-0002-0553-0137), Caroline L. Monteil (0000-0002-2834-6834), Christopher T. Lefevre (0000-0002-1692-0245).

Author contributions: D.M.C., A.J., N.M., D.F. K.B., C.L.M., and C.T.L. designed research; D.M.C., A.J., N.M., K.B., Ro.B., W.W., G.A.P., M.K.S., P.E.D.S.R., and C.T.L. performed research; F.S.P., Ra.B., D.F., A.K., H.L.G., and E.P. contributed new reagents/analytic tools; D.M.C., A.J., N.M., K.B., P.E.D.S.R. and C.T.L. analyzed data; D.M.C., C.L.M., and C.T.L. wrote the paper; N.M., P.E.D.S.R., G.A.P., D.F. and K.B. contributed partial writing.

37 The authors declare no competing interest.

38 **Classification**: Biological Sciences (Major), Biophysics and Computational Biology (Minor)

39

40 **Keywords**: collective magnetotaxis, magnetosomes, symbiosis, biomineralization, holobiont,
41 magnetotactic bacteria

42

43 **Abstract**

44 Over the last few decades, symbiosis and the concept of holobiont – a host entity with a population of
45 symbionts – have gained a central role in our understanding of life functioning and diversification.
46 Regardless of the type of partner interactions, understanding how the biophysical properties of each
47 individual symbiont and their assembly may generate collective behaviors at the holobiont scale remains a
48 fundamental challenge. This is particularly intriguing in the case of the newly discovered magnetotactic
49 holobionts (MHB) whose motility relies on a collective magnetotaxis (*i.e.*, a magnetic field-assisted
50 motility guided by a chemo-aerotaxis system). This complex behavior raises many questions regarding
51 how magnetic properties of symbionts determine holobiont magnetism and motility. Here, a suite of light-
52 , electron- and X-ray-based microscopy techniques (including X-ray magnetic circular dichroism
53 (XMCD)) reveals that symbionts optimize the motility, the ultrastructure and the magnetic properties of
54 MHBs from the microscale to the nanoscale. In the case of these magnetic symbionts, the magnetic
55 moment transferred to the host cell is in excess (10^2-10^3 times stronger than free-living magnetotactic
56 bacteria), well above the threshold for the host cell to gain a magnetotactic advantage. The surface
57 organization of symbionts is explicitly presented herein, depicting bacterial membrane structures that
58 ensure longitudinal alignment of cells. Magnetic dipole and nanocrystalline orientations of magnetosomes
59 were also shown to be consistently oriented in the longitudinal direction, maximizing the magnetic
60 moment of each symbiont. With an excessive magnetic moment given to the host cell, the benefit
61 provided by magnetosome biomineralization beyond magnetotaxis can be questioned.

62

63 **Significance Statement**

64 Symbiosis between a motile microeukaryotic host and dozens of non-motile, surface-attached magnetic
65 bacterial symbionts was recently discovered, where the host acquires geomagnetic field-guided navigation
66 thanks to chains of ferrimagnetic nanoparticles (within organelles called magnetosomes) produced by the
67 bacteria. Our findings reveal magnetic dipoles of each magnetosome chain consistently align and thus
68 efficiently confer a large magnetic moment to the host cell. Remarkably, the calculated magnetic moment

69 is greatly in excess of that required to gain a magnetotactic advantage. These results show an optimization
70 of collective magnetotaxis during the course of evolution owing to the three-dimensional organization and
71 magnetic properties of bacteria but also raise the question on the magnetosome's function beyond
72 magnetic field guidance since they abundantly cover the host.

73

74 **Introduction**

75 Species are adapted to their environment thanks to the heritable changes in their structure, physiology,
76 locomotion, dispersal, reproduction and other behaviors that have passed the filter of natural selection
77 over generations. Several evolutionary forces may trigger these changes and shape biodiversity, among
78 which symbiosis has gained a lot of recognition in recent decades (1). By creating intimate and long-term
79 physical interactions, different organisms may rapidly acquire a variety of functions, ranging from
80 detoxification, to cell defense, motility and, in most cases, metabolic abilities. Together, symbiotic
81 microorganisms form a single ecological unit, called a holobiont (2), whose functioning allows its
82 partners/bionts to extend their ecological niche and colonize otherwise previously inaccessible habitats.
83 The symbiont integration level may vary from a simple attachment to cell surfaces to their integration into
84 the cell cytoplasm. In the most extreme cases of endosymbiont host integration, symbiosis can even lead
85 to the creation of new organelles and genome transfer to the host nucleus, often illustrated by the
86 eukaryogenesis (3, 4).

87 Symbioses are established between organisms from all domains of life and have been mostly
88 studied in macrobial systems involving multicellular eukaryote models (5, 6). Symbioses in the microbial
89 world are also widespread but less known even though they are of prime interest to gain insights into the
90 mechanisms driving life complexification and evolution. However, observation and characterization of
91 microbial symbioses have been challenging for many years; most symbionts defy commonly applied
92 enrichment and cultivation techniques (1). Even if metagenomic and single-cell genomic approaches may
93 now circumvent some of these issues by enabling the reconstruction of genomes from symbionts in their
94 natural habitats (7), *in silico* approaches do not entirely reveal the holobiont structure and behavior.
95 Therefore, interrogating the physical properties of microbial symbiotic systems may bring insights on
96 mechanisms or interactions that have shaped biodiversity. Improvements in micro- and nano-scale
97 analytical instrumentation and sample preparation strategies over the past few years have boosted
98 biophysical research, permitting microbial holobiont studies from the single cell level to organelle level
99 (8). For instance, approaches such as synchrotron-based X-ray spectromicroscopy imaging, focused ion
100 beam (FIB)-scanning electron microscopy, and cryo electron microscopy (and associated cryo-

101 preparation protocols) have made it possible to rigorously examine the ultrastructure and organization of
102 individual cells, while other techniques such as nanoscale secondary ion mass spectrometry (NanoSIMS)
103 can trace the metabolic exchanges to decipher intra-/inter-cellular chemical interactions (9).

104 Microbial holobionts may adopt behavior patterns almost completely determined by the
105 symbionts. Cell to cell interactions between bionts generate an emergent collective behavior that may
106 change the mechanical, biological and physicochemical properties of each partner over generations.
107 Although debated amongst evolutionary biologists (10, 11), a microbial holobiont can nevertheless be
108 seen as a main unit of selection. As such, any cell or organelle function, structure and organization
109 optimizing the collective behavior may therefore be selected in a given environmental context. These
110 evolutionary processes may create a complete dependency in some biological systems, which is well
111 illustrated by mitochondria and chloroplast evolution (12). Not all symbioses are obligatory, but most of
112 them involve a metabolic dependency from at least one of the partners. Such is the case with the
113 endosymbiotic methanogenic archaea or denitrifying bacteria in hydrogenosome-bearing protists (13, 14).
114 Other benefits can rely on structural integrity or locomotion. Indeed, similar to other biological systems
115 (15), symbiont interactions can generate a collective motion. For example, some flagellates are mobile
116 owing to thousands of ectosymbiotic bacteria (*e.g.*, spirochetes) anchored to the host membrane, which
117 ensure its movement with their flagella (16).

118 Recently, a new collective behavior was described in a group of microbial holobionts ubiquitous
119 in anoxic marine sediments. The functioning of this holobiont relies on a multi-scale cooperation between
120 a flagellate, euglenozoan protist and dozens of non-flagellated, sulfate-reducing bacteria of the
121 *Deltaproteobacteria* class, which biomineralize magnetic nanocrystals (17). First, the host and symbionts
122 interdependency relies on metabolic exchanges. Some of them were identified based on the host
123 ultrastructure and ectosymbiont genome (17). Their syntrophy is most likely based on the transfer of
124 molecular hydrogen produced by mitochondria-derived organelles, called hydrogenosomes, from the host
125 to the bacteria that use it to reduce sulfate. Second, these holobionts harbor a peculiarity compared to
126 other symbiotic systems described in such habitats: they adopt a collective magnetotaxis, (*i.e.*, a motility
127 guided by a chemo-aerotaxis system and geomagnetic fields). Similar to magnetotactic bacteria (MTB)
128 (18, 19), magnetotactic holobiont (MHB) motility is guided by geomagnetic fields, which is assumed to
129 facilitate their positioning in preferred ecological niches, just below the oxic-anoxic boundaries of
130 sediments. The passive alignment in a magnetic field is ensured by ectosymbionts through the
131 biomineralization of chained lipidic vesicle-encapsulated ferrimagnetic nanocrystals called
132 magnetosomes. Experimental observations evidenced that the magnetic guidance was influenced by
133 oxygen gradients, while a nearly complete genome of biomineralizing bacteria showed complete loss of

sensing and motility machinery (17). Therefore, magnetotaxis appears to emerge from the collective effects of magnetosome chain positioning from ectosymbiotic bacteria and the host motility and chemo-aerotaxis.

The discovery of MHBs raises many questions regarding the magnetic properties of this collective behavior and how it echoes the magnetic properties developed in free-living prokaryotes (*i.e.*, MTB). As long as magnetotaxis provides a selective advantage (20), the function is supposed to have been optimized over the time of holobiont diversification. If so, to what extent did holobionts converge toward the same motility behavior in response to chemical gradients and magnetic fields as in prokaryotes? And since cell polarity, flagella organization, magnetosomes arrangement, number and polarity impact magnetic behavior in free-living MTB (21–25), how are these features organized by symbionts to maintain a successful magnetic guidance at the scale of the consortium?

Here, we employ light-, electron- and X-ray-based microscopy techniques to characterize the motility, the ultrastructure and the magnetic properties of MHBs. The calculated magnetic dipole of MHBs from magnetic field-based motility assays was found to be more than two orders of magnitude greater than free-living MTB, an amount clearly in excess of that required to gain a magnetotactic advantage. Microscopy imaging of MHB ultrastructure (using scanning electron microscopy (SEM), transmission electron microscopy (TEM), scanning-TEM (STEM), cryo soft X-ray tomography (cryo-SXT)) and spectroscopic investigation of magnetosome magnetic properties (using X-ray magnetic circular dichroism (XMCD)) confirm a cohesive organization of ectosymbiotic cells and consistent magnetic dipole direction of magnetosome chains relative to the host, which confers an ultrasensitive magnetotaxis property to the holobiont. Lastly, unlike previously reported magnetite (Fe_3O_4) crystal morphology in *Deltaproteobacteria*, we discovered that ectosymbiotic bacteria produce rhomboidal dodecahedron-like particles. From the microscale to the nanoscale, the results support hypotheses that the positioning, organization and number of ectosymbiotic cells and magnetosome chains are overly optimized by symbionts to insure a collective magnetotaxis similar to the magnetotaxis behavior observed in MTB. Furthermore, these results stimulate the debate of magnetosomes function beyond magnetotaxis since the additive magnetic moment is orders of magnitude in excess of that required for effective magnetotaxis.

164 **Results**

165 ***Magnetotactic holobionts have a magnetotactic behavior similar to free-living magnetotactic bacteria***

166 Since the first description of magnetotactic holobionts (MHBs) (17), we have continuously collected
167 samples in Carry-le-Rouet, France (Mediterranean Sea), to have a sufficient number of south-seeking
168 MHBs to perform an extensive characterization of their ultrastructure and magnetotaxis. SEM and light
169 microscopy observations show two thick flagella, each measuring about two to three times the length of
170 the cell body, which is typical in Euglenids (Movie S1 and Fig. 1A). Transverse section of the flagella
171 shows a canonical '9+2' microtubule axoneme structure (Fig. S1) (26). SEM and TEM indicate that both
172 flagella emerge from a large depression (Fig. 1) from the anterior pole where the protist is only partially
173 covered by few magnetic ectosymbiotic bacteria (MEB) in contrast to the rest of its cell body (Fig. 1D
174 and E). SEM observations at low electron energy show magnetic ectosymbiotic bacteria (MEB) densely
175 cover the surface of the protist (Fig. 1B), while imaging at higher electron energy confirmed that they
176 contained structurally-aligned nanoparticle chains (Fig. 1C).

177 We assessed the extent to which collective magnetotaxis evolved towards the same motility
178 behavior as the one observed in single-celled MTB. Magnetic moments of MHBs were obtained by
179 analyzing their U-turn motion (Fig. 2A and B present optical image of MHB in recorded video and
180 schematic of U-turn experiment, Fig. S2 presents additional extracted motility parameters), which relates
181 the radius and turning time of MHBs upon external magnetic field reversal using the following equation
182 (27):

183 $$\tau_{Uturn} = \frac{A}{M \cdot B} \cdot \ln\left(\frac{2 \cdot M \cdot B}{k_B T}\right) \qquad (1)$$

184 Here, τ_{Uturn} corresponds to the time the MHB take to make a U-turn upon switching the applied magnetic
185 field (B); M is the magnetic moment of the MHB; k_B corresponds to the Boltzmann constant and T the
186 temperature at which the experiment was performed (25°C). A is a constant related to a viscous torque.
187 By considering the MHB shape to be an ellipsoid (17), it is defined as:

188 $$A = \left(\frac{16}{3}\right)\pi\eta c^3 \cdot \left[\frac{1}{2} \cdot ln\left(\frac{(a+c)}{(a-c)}\right) - \frac{(a*c)}{b^2}\right] \qquad (2)$$

189 Where η corresponds to the media viscosity (*i.e.*, Mediterranean Sea viscosity at 25 °C), a (10 µm) and b
190 (5 µm) are the major and minor axes of the ellipsoid, respectively, and $c^2 = a^2 - b^2$. The MHB U-turn
191 time (τ_{Uturn}) was determined by tracking the U-turn trajectory and then plotting the first derivative,

192 corresponding to the instantaneous velocity (Fig. 2C), where the change in sign corresponds to the change
193 in direction. Then, by taking the time difference between maximum and minimum peaks (shown in Fig.
194 2D), the value of τ is obtained and therefore M can be calculated from equation (1). A set of MHB U-turn
195 trajectories (n = 22) were tracked to calculate τ_{Uturn} and M. We obtained an average absolute value of the
196 magnetic moment $M = 1.8 \pm 0.8 \times 10^{-13}$ A·m^2. Similar magnetic moments have been found for *Candidatus*
197 Magnetoglobus multicellularis (between $9 \pm 2 \times 10^{-15}$ and $20 \pm 3 \times 10^{-15}$ A·m^2 (28)) and magnetotactic
198 protists (6.7×10^{-12} A·m^2 (29) and $2.5 \pm 1.2 \times 10^{-13}$ A·m^2 (30)). As a comparison, the magnetic moment of
199 *Magnetospirillum gryphiswaldense* (MSR-1) was previously determined to be $2.5 \pm 0.5 \times 10^{-16}$ A·m^2 (31)
200 or around 7.7×10^{-16} A·m^2 by direct measurement of the magnetosome chain using magnetic tweezers
201 (32). Similar magnetic moments have been found for other species of MTB as well (33, 34).

202 ***Ectosymbiotic cells are parallel to each other and oriented along the long axis of their protistan host***

203 To obtain a global understanding of MEB organization in their native-state configuration (*i.e.*, without
204 congealing artifacts from fixation processes), MHB samples were vitrified for cryo soft X-ray
205 tomography (cryo-SXT) imaging. Cryo-SXT offers a relatively deep penetration and enhanced natural
206 contrast of biological materials in the water window (*i.e.*, X-ray absorption from C and N K-edges)
207 without chemical fixation or staining. Fig. 3A presents tomogram reconstructed slices of the vitrified
208 MHB captured with an incident energy of 520 eV (raw X-ray image of this MHB and tilt-series images
209 are shown in Fig. S3, see Movie S2 for tomogram video). Owing to a voxel size of (12 nm)^3 and the high
210 density of magnetite nanocrystals, magnetosome chains were distinguishable in MEB from tomography
211 virtual slices and were assigned during volume segmentation (see Materials and Methods). The
212 segmentation of the entire volume reconstruction is presented in Fig. 3B with magnetosome chains in red,
213 MEB membrane in yellow (only partially reconstructed due to limited contrast in the tomographic
214 volume), protistan host in cyan (*i.e.*, outer membrane and intracellular compartments) and dense
215 intracellular granules in white (identified as phosphorus- and calcium-rich granules using X-ray energy-
216 dispersive spectrometry (XEDS); Fig. S4). The bottom side of the MHB (in contact with the carbon film
217 of TEM grid) was flattened likely due to sedimentation or the vitrification process. This can be observed
218 from the “front” and “side” views of the reconstructed model (Fig 3B, right panels). When considering
219 the magnetosome chains in red; Fig. S5 shows only this reconstructed volume and the protistan host. We
220 note the magnetosome organization has a general similarity to that identified with multicellular
221 magnetotactic prokaryotes (MMPs) (35, 36); magnetosomes are found at the exterior of the consortium
222 and they align in the direction from pole to pole. For MMPs, however, magnetosomes organize into
223 chain-like clusters, not distinct chains as for the MHB.

224 Thin-sections of MHB confirmed that the protistan host is covered by one layer of longitudinally
225 arranged, curved rod-shaped ectosymbiotic bacteria (Fig. 1D and 4A and B). Bacterial cells are localized
226 within an invagination of the outer membrane of their host (Fig. 4A-C). Such channel-like structures may
227 help the bacteria to maintain position at the surface of the eukaryotic host and increase their surface
228 contact with the host for increased transfer of material for chemical symbiosis-related exchanges.
229 Transversal sections of ectosymbionts revealed a consistent and unique morphology (Fig. 4A-E). As
230 previously reported (17), transversal sections indicate the presence of wing-like structures in all
231 ectosymbionts. Here, we show that these structures are protrusions from the external membrane only (Fig.
232 4C-E) with one of the wing structures often below and the other above neighboring bacterial cells (Fig.
233 4D). These structures could also be observed from SEM images where they appear as tapered edges (Fig.
234 S6). The linking of adjacent wing structures may help to improve ectosymbiotic cells cohesion.
235 Longitudinal and transversal sections also reveal the presence of vesicles (*i.e.,* round structures) between
236 bacteria that could also be involved in the fixation of the symbionts (Fig. 4c-f). These vesicles could also
237 be part of the communication between MEB to coordinate their activities such as cell division. Similar to
238 the vesicles previously observed in MMPs (21). The presence of the ectosymbiotic bacteria in the vicinity
239 of hydrogenosomes produced by the protist was also confirmed (Fig. 4C and D).

240 Transversal sections indicate that magnetosomes are always positioned in the lower half of the
241 MEB cell body, closer to the host (Fig. 4A-E) or on side of the MEB with shorter inner curvature radius.
242 Similar magnetosome positioning at midcell was previously reported in the free-living *Magnetospirillum*
243 *gryphiswaldense* MSR-1. It was shown that the cytoskeletal determinant CcfM links the magnetoskeleton
244 (*i.e.*, magnetosome-specific cytoskeleton produced by specific proteins such as MamK) to cell
245 morphology in regions of inner positive-cell curvature (22). In the case of MEB, such positioning of the
246 magnetosome chain could represent an advantage for optimizing the magnetic moment of the MHB.
247 Although the genome of MEB did not contain any orthologue of CcfM, it is possible that another
248 molecular pathway is involved in magnetosome positioning in MHBs.

249 All magnetosome chains are aligned along the long axis of the host cell. Towards the front or
250 back of the host, magnetosome chains are tilted inward (*i.e.*, following the curvature of the host cell),
251 indicating a close contact between MEB and the surface of the host cell. From cryo-SXT volume
252 reconstruction (Fig. 3) and TEM thin sections (Fig. 4), parallel magnetosome chains are typically spaced
253 0.5-1 µm apart. Considering the potential for interchain interactions to influence the ensemble magnetic
254 properties, micromagnetic calculations of simulated magnetosome chain structures were conducted using
255 MERRILL (v1.6.4) (see Materials and Methods) (37). Based on the average particle size, spacing and
256 number of particles per chain as measured by TEM, a chain of 25 rhomboidal dodecahedral nanocrystals

257 (see section below for the characterization of the nanocrystal shape) with a mid-sphere diameter of 60 nm
258 and 10 nm spacing between grains was built to model the adjacent stray fields. Based on this calculation
259 (Fig. S7), stray fields at least 1 µm from the chain (in both parallel and perpendicular directions) are
260 consistently more than three orders of magnitude weaker than the remnant magnetization (M_{rs}) of the
261 entire chain (8.4×10^{-16} A·m^2, see Materials and Methods), ruling out significant interchain interactions.
262 Moreover, the magnetic moment for one of the modelled magnetosome chain structures is high enough to
263 overcome Brownian motion at 20 °C in a magnetic field of 10 µT. To impart a magnetotactic advantage
264 for MHBs over other microorganisms of similar size (*i.e.*, a net average bias (> 50 % of the population) of
265 *n* cells aligned with the magnetic field direction against randomized orientation caused by Brownian
266 motion), we considered how the magnetic moment of magnetosome chains decrease because of their
267 bending to follow curvature of the host cell (Fig. S8). Regardless of these few chains at the extreme ends
268 of the cell, which are highly curved, we estimate that net cell magnetization from only a few chains
269 positioned close to the middle section of the host is sufficient to confer magnetotaxis on the MHB (see
270 Fig. S8 and Materials and Methods). The total magnetic moment of the holobiont being 1.8 x 10^{-13} A·m^2
271 and that of a single magnetosome chain 8.4 x 10^{-16} A·m^2, with most of the magnetosome chains aligned
272 parallel to each other, our model would indicate there are about 215 chains attached to the host which is
273 consistent with microscopy observation (100-200 MEB/holobiont) (17).

274 ***Magnetic moments of magnetosome chains align to enhance magnetotaxis ability of their host***

275 Considering magnetosome chain organization, negligible interchain interaction, and the above-calculated
276 ensemble magnetic moment of MHBs, the magnetic moment of each chain should contribute
277 independently and additively to the magnetic moment the host cell experiences. This assumption was
278 tested by measuring the native-state magnetic moment of individual chains *via* scanning transmission X-
279 ray microscopy with X-ray magnetic circular dichroism (STXM-XMCD) in the absence of applied
280 magnetic fields.

281 For STXM-XMCD sample preparation, MHB samples were magnetically extracted from
282 environmental samples using weak magnetic fields (see Materials and Methods). Further, when collecting
283 XMCD, no magnetic fields were applied on the sample. Instead, the sample was tilted ~30° to the normal
284 plane to probe the intrinsic magnetization of each magnetite nanocrystal (Fig. S9A and B for experimental
285 setup) (38). MHBs with magnetosome chains positioned perpendicular to the axis of rotation of the
286 sample holder were analyzed to optimize the XMCD signal. This is because the magnetization easy axis
287 is typically aligned along the magnetosome chain direction, *i.e.,* <111> crystallographic direction of
288 magnetite (see below for high-resolution TEM analyses; (39–41)). Furthermore, it was important to

identify MHBs that had intact flagella, so that a correlation between the magnetization of magnetosome chains and the swimming direction (*i.e.*, south-seeking) could be assessed.

Fig. 5A and B present STXM images of two different MHBs positioned in opposite directions and observed at 710 eV (*i.e.*, at the Fe L_3-edge), where magnetosome chains are most visible against the host cell. At this energy, it is also possible to observe the flagella of the deposited MHBs (confirmed with optical microscopy). We then utilized three energy points in the Fe L_3-edge absorption region that show the maximum XMCD response (708.8, 709.8 and 710.7 eV, see Fig. S9C for identification of these energies) to collect maps with both circular polarizations of incident X-rays (circular polarized left (CPL) and right (CPR)). Higher resolution analyses on regions of interest for the first MHB show differences in signal intensity between circular polarizations (Fig. 5C). Based on the tilt direction of the sample holder, the orientation of MHB (*i.e.*, swimming direction) and the circular polarization, the resulting color in the XMCD difference maps indicates the direction of magnetization. Here, the red color indicates magnetization in the right direction (Fig. 5C), while blue indicates magnetization in the left direction (Fig. 5D). As seen from the presented XMCD difference maps, the projected magnetization of magnetosome chains is mostly uniform, pointing towards the flagella end of the MHB. This was confirmed by measuring another MHB with the flagella on the opposite side (Fig. 5B and D). In total, three MHB were analyzed (Fig. S10 shows the third MHB without chemical fixation), consistently demonstrating magnetic dipoles of magnetosome chains are in the same direction among ectosymbionts with their magnetic south pole pointing toward the flagella, thus optimizing the swimming direction of the protistan host toward the south. This suggests magnetic dipole direction is maintained for dividing ectosymbionts. A similar conservation of magnetic dipole direction relative to consortium structure during division has also been identified for multicellular magnetotactic prokaryotes (MMPs) (42).

An inversion of individual magnetic dipole direction against the overall magnetization vector was discovered on a few occasions, which occurs in the middle or at the end of magnetosome chains. These inversions are evident by the alternating red-blue regions in the CPL-CPR difference maps (Fig. 5C). These inversions also confirm the magnetic field strength used to extract MHBs from collected sediment did not disturb native magnetic moments of magnetosomes. The crystalline orientation of magnetosome particles in one inversion region was revisited and examined using scanning transmission electron microscopy high-angle annular dark field (STEM-HAADF) imaging. Fig. S11 shows the STXM region in Fig. 5A (top left region, purple frame) and plots the <111> alignment of individual particles as found from FFT and stereographic projections. This demonstrates the consistent alignment of magnetite's easy axis <111> with the chain direction despite the inversion of magnetic dipoles.

321 We then performed further HR-TEM analyses of individual magnetosomes for three MEB from
322 three different MHBs, confirming expected {111}, {100} and {110} faces of magnetite nanocrystals (Fig.
323 6) and identifying the nanocrystal orientation in chain structures. The <111> crystallographic direction of
324 each particle was almost systematically aligned along the chain length. This is consistent with the
325 orientation generally observed for individual MTB biomineralizing prismatic magnetite (41). Upon close
326 inspection of several individual magnetosomes, the shape of most magnetite nanocrystals is best
327 described as a rhomboidal dodecahedron (Fig. S12 and S13), a morphology that exhibits only {110}
328 faces. Fig. S14 and S15 present additional HR-TEM analyses of individual particles and demonstrate the
329 consistent <111> alignment with chain direction and further this unexpected nanocrystal shape for
330 magnetite. This crystallographic form of magnetite from a magnetosome-producing bacterium of the
331 *Deltaproteobacteria* class is unanticipated, which suggests previous studies that correlated the nanocrystal
332 morphology formed by a bacterium and its phylogenetic position should be reconsidered (41, 43, 44).

333

334 **Discussion**

335 Many microorganisms, including bacteria, microeukaryotes and archaea, live together permanently or at
336 least transitorily by forming microbial holobionts. These intimate relationships must not only satisfy
337 metabolic requirements, but their physical assembly must maintain, and even improve, holobiont integrity
338 and motion. This study utilized a suite of imaging and characterization tools to generate insights on one of
339 the most fundamental cases of collective magnetotaxis known, ranging from motility in magnetic fields,
340 three-dimensional organization of magnetosome chains around the host cell, polarity of magnetic dipoles,
341 ultrastructure of bacterial cells at the surface of the host, down to the morphology of magnetite
342 nanocrystals. Based on the different scales of our analysis, the MHB studied here is a model system apt to
343 be investigated with the electron and X-ray based imaging, which provide the adequate spatial resolutions
344 to capture the intricate organization at both cellular and nanoparticle size regimes. Based on MHBs, what
345 can symbiosis research gain from such collective motion and physical characterization studies?

346 The first finding is that a similar field-guided motility has emerged independently in free-living
347 single-celled MTB and in microeukaryotes through symbioses, although the magnetosome organelle has a
348 common prokaryotic origin. The magnetic moment determined using U-turn analysis was $1.8 \pm 0.8 \times 10^{-13}$
349 $A \cdot m^2$ (n = 22), a value more than two orders of magnitude higher than the magnetic moment of a single
350 MTB (45–49). This magnitude of magnetic interaction with the geomagnetic field is in excess for the
351 MHB. Our micromagnetic calculations on the magnetic dipole strength of simulated magnetosome chains

352 and the size and shape of the entire holobiont estimate (considering Brownian motion at 20 °C) that only
353 a few magnetosome chains – not dozens – positioned longitudinally along the mid-section of the host cell
354 would be sufficient for the protist cell to gain a magnetotactic advantage (in fields > 10 μT) over other
355 motile microorganisms of similar size (see Fig. S8 and Materials and Methods). It was then hypothesized
356 from this calculation and our characterization of the MHB that perhaps more magnetosome chains were
357 necessary during periods of weak geomagnetic field strength in Earth's history. However, even with a
358 field strength of ~1 μT, only a few additional magnetosome chains contributing to the additive magnetic
359 moment of a holobiont would be required (Fig. S8). Therefore, the dozens of magnetosome chains that
360 cover the MHB are greatly in excess of what is required for effective magnetotaxis. Similar observations
361 have been made in the magnetotactic multicellular prokaryotes where their magnetic moment was
362 optimized to a large degree (28, 36, 42).

363 At the magnetosome level, we observed a uniformity of magnetic dipole direction in MEB.
364 However, as presented in Fig. 5C, inversion of magnetosome magnetic dipole was detected on a few
365 occasions, although its origin could not be determined by the present work. We note that magnetic dipole
366 inversions have been reported for MTB strains MV-1 and AMB-1 when a similar XMCD-STXM
367 measurement was performed (38, 50). In the case of *Magnetospirillum magneticum* (AMB-1) studies,
368 inversion of an entire magnetosome chain segment was found for a mature cell, whereas out-of-plane
369 magnetic dipoles were found for recently biomineralized magnetosomes. For MHB, the alternating
370 inversions of individual magnetosomes do not appear to originate from immature magnetosomes as these
371 particles are found mid chain, spaced closely to other magnetosomes, and are of average particle size.
372 Regardless of this irregularity to be further understood, the consistent alignment of chain magnetic
373 dipoles is an indicator of highly controlled cell division (24) and appropriation of chains on the host cell
374 to maintain the maximum magnetic moment. This is in contrast to a recent finding by Leão *et al.* (30)
375 where bundles or clusters of bullet-shaped magnetosomes were discovered in a flagellated protist that
376 showed a seemingly random organization of magnetosome magnetic dipoles.

377 TEM examinations reveal additional interesting features: bionts have evolved specific structures
378 and three-dimensional organization to optimize holobiont stability and hydrodynamics. Chains and MEB
379 cells are parallel to the microeukaryote/holobiont motility axis, and extracellular vesicles and MEB wing-
380 like protrusions seem to stick and arrange bionts together in this orientation. This reveals that beyond the
381 chemical symbiosis previously described between host and ectosymbiotic bacteria (17), the holobiont
382 collective behavior emerges from physical interactions between biological interfaces (positioning and
383 structural integrity of ectosymbiotic bacteria on the host) and between magnetic dipoles and the
384 geomagnetic field (retention of magnetic dipole direction with respect to direction of motility). These

385 physical constraints may act on biology to drive the adaptive evolution of the holobiont. Without
386 complying to these physical restrictions, the consortium's persistence would be challenged.

387 Such a biological constraint exerted by magnetotaxis suggests an important ecological role for the
388 holobiont. As hypothesized previously (17), the host benefits from the same advantages as MTB in
389 chemical gradients, namely, finding more easily optimal chemical redox conditions in fluctuating
390 environments. Collective magnetotaxis may thus optimize holobiont efficiency for nutrient acquisition or
391 avoidance of toxic substances. Sharing the function with the protistan host may avoid the metabolic
392 burden of synthesizing flagellar components for MEB, the energetic expense of fueling flagellar motors
393 and the exposure of some molecules that could be recognized by predators. More environmental and
394 genomic data will resolve the adaptive history, but can the biophysical characterization of MHBs give
395 insights into the syntrophy itself or the fundamental role of magnetosomes in MTB? Attention has been
396 paid to the geolocation function of magnetosomes to explain the emergence of such a biomineral and
397 organelle (43, 51, 52). However, if this primary function requires only few magnetosome chains in
398 MHBs, then why is the magnitude of magnetic interaction with the geomagnetic field excessive, and why
399 do MEB continue to spend energy to produce such an excess number of magnetosomes? Here, MHBs
400 provide further evidence that magnetosomes might also be involved in metabolic aspects and possibly
401 syntrophy. Similar to what has been proposed for MTB, MEB could act as a battery to fuel the protist
402 (53). The close vicinity of magnetosomes to the protist's external membrane could evidence a possible
403 traffic of energy from prokaryotic cells toward the eukaryotic host, similar to how hydrogenosomes
404 function but in the opposite direction (*i.e.,* fueling the MEB with H_2) (17, 54). Another hypothesis
405 explaining such a large amount of magnetosomes in MHBs is an antioxidant defense. Indeed, it was
406 shown in model MTB strains of the *Magnetospirillum* genus that magnetosomes exhibit a peroxidase-like
407 activity (55, 56). Magnetosomes were proposed to decrease and eliminate reactive oxygen species (ROS)
408 in the cell. Thus, in MHBs, ectosymbiotic cells could serve as a sink for the ROS produced by their
409 protistan host during metabolic activity or exposure to oxygen (57). Although little is known about the
410 physiology of this MHB protist and its closest relatives, it is possible that they require a high
411 concentration of iron for metabolic needs. Since MTB are known to be very efficient in the uptake of iron
412 (58), the protist could benefit from the iron uptake by its symbionts with the transfer of iron from the
413 ectosymbionts toward the protist.

414 Magnetotaxis in MTB is usually described as a passive orientation and active swimming along
415 the Earth's magnetic field lines thanks to magnetosomes and to flagella, respectively (59). However, it
416 was shown that a potential magnetic sensing, *via* the widely used chemotaxis mechanism, might be
417 actively involved in magnetotaxis (60). In *Magnetospirillum magneticum* AMB-1, a methyl-accepting
418 chemotaxis protein (MCP) appears to interact with the protein MamK involved in magnetosome chain

419 formation. This finding led to the hypothesis that the magnetic torque applied on the magnetosome chain
420 might be relayed by MamK and transferred to MCPs at the cell poles *via* specific interactions between
421 them. The chemotaxis signal transduction system may then take over the subsequent response of the cell.
422 In MHBs, it is likely that such signal transduction system between the MEB magnetosome chains and the
423 host flagellar motor is absent as it was shown that none of the genes encoding classical chemotaxis
424 pathways were detected in the genome of MEB (17). Thus, to overcome potential swimming deviation
425 against the Earth's magnetic field, a last hypothesis to consider is that the higher the number of
426 magnetosome chains, the better MHBs can maintain a swimming direction parallel to the magnetic field.
427 Future studies that inspect MHBs under laboratory-based conditions and their diversity in aquatic
428 environments will hopefully reveal more on the function of magnetosomes for eukaryotes. The discovery
429 of collective magnetotaxis has opened up a new interdisciplinary field of study in biology and biophysics
430 to answer the questions this symbiosis between eukaryotes and prokaryotes generates on their evolution
431 (*i.e.,* were ectosymbiotic bacteria originally recruited with the ability to produce magnetosomes or was
432 the formation of magnetosomes acquired by the bacteria after they started their symbiosis with their
433 host?) and functioning (*i.e.,* what major advantages does the protist obtain by carrying dozens of
434 biomineralizing bacteria on its surface?).

435

436 **Materials and Methods**

437 **Sample collection and light microscopy observations.** Samples were collected by free-diving at a water
438 depth of 0.5-2 m in the Mediterranean Sea, in Carry-le-Rouet (43.334222°N, 5.175278°E). One-liter glass
439 bottles were filled to about 0.3-0.5 of their volume with sediment, then filled to their capacity with water
440 that overlaid the sediment. Air bubbles were excluded. Once in the laboratory, samples were stored under
441 dim light at room temperature (~ 25 °C). South-seeking magnetotactic holobionts were concentrated by
442 placing a magnetic stirring bar (~ 10 mT) next to the bottles, above the sediment-water interface for 2 h.
443 Examination of magnetically concentrated cells was carried out using the hanging drop technique (61)
444 under a Zeiss Primo Star light microscope equipped with phase-contrast and differential interference
445 contrast optics. The local magnetic field used to determine magnetotaxis was reversed by rotating the
446 stirring bar magnet 180 ° on the microscope stage.

447 **Movement and magnetotactic response analysis**. A customized magnetic microscope equipped with a
448 triaxial Helmholtz coilset and controller (C-SpinCoil-XYZ, Micro Magnetics Inc.) and a Andor Zyla 5.5
449 high speed camera was used (62). The 3D-axis Helmholtz coils can generate DC magnetic fields with a

450 precision of 5 % of Earth's magnetic field (± 2.5 μT). Using the setup, we programmed the switching of
451 the magnetic field between -3.5 and +3.5 mT for the U-turn. For U-turn measurements, the magnetic field
452 was fixed for 2 s before switching. The switching was repeated to collect at least three U-turns in the field
453 of view. The trajectories and U-turn of 22 MHB were extracted and smoothed by a tracking script written
454 in python and based on the OpenCV Object Tracking Algorithms with the CSRT tracker. The data is
455 smoothed by a convolution-based smoothing approach. For both trajectory and U-turn measurements, a
456 20X objective (N.A. 0.45) was used. The mathematical relation to calculate the MHB magnetic moment
457 from the U-turn time are described in the main text by equations (1) and (2). The fsolve function from
458 Octave/Matlab was used to obtain M from equation (1). Data fitting was done by the intrinsic fitting
459 functions of OriginPro, Version 2016 (OriginLab Corporation, Northampton, MA, USA).

460 **Scanning electron microscopy (SEM).** Magnetically concentrated MHB were fixed in a solution of 1 %
461 paraformaldehyde and deposited on a glass coverslip coated with poly-L-lysine and stored at 4 °C. Before
462 the observation, the sample was dehydrated in successive ethanol baths (50 %, 70 %, 96 %, 100 %) then
463 processed through critical point drying (CPD) (Leica EM CPD300) before coating with carbon (Leica EM
464 SCD500). Images were collected in the backscattered and secondary electron modes using a Zeiss Ultra
465 55 FEG-SEM operating at 1–10 kV, a working distance of 4 mm and an aperture of 10–60 μm.

466 **Transmission electron microscopes (TEM).** TEM was used on ultrathin sections to characterize the
467 ultrastructure of the magnetotactic holobionts. Thin-sectioned samples were prepared from magnetically
468 concentrated protists fixed in 2.5 % (w/v) glutaraldehyde in sodium cacodylate buffer (0.1 M, pH 7.4) and
469 kept at 4 °C for at least 24 h. Due to the low biomass of MHB, fixed cells were embedded in a small
470 agarose plug to facilitate their transfer in the different solutions before the inclusion in resin. Cells were
471 post-fixed one hour with 1 % (w/v) of osmium tetroxide. Cells were then dehydrated with successive
472 ethanol baths (30, 50 70, 90, 100 %) with increasing concentrations and finally embedded in the resin
473 (Epon 812). Sections (40 nm thick and 3 mm long) were cut with the UC7RT ultramicrotome (Leica
474 Microsystems GmbH), deposited onto TEM copper grids and stained with uranyless solution for 10 min
475 and Reynolds lead citrate 3% for 3 min. Electron micrographs were recorded with a Tecnai G2 BioTWIN
476 (FEI Company, Eindhoven, Netherlands) equipped with a CCD camera (Megaview III, Olympus Soft
477 imaging Solutions GmbH, Münster, Germany) with an accelerating voltage of 100 kV. The sizes of
478 magnetosomes were measured from TEM images using the ImageJ software (v1.48).

479 **High-resolution transmission electron microscopes (HRTEM) and X-ray energy-dispersive**
480 **spectrometry (XEDS).** HRTEM was performed on cells directly deposited onto TEM copper grids
481 coated with a carbon film. HRTEM and z-contrast imaging in the high-angle annular dark field (STEM-

482 HAADF) mode, and elemental mapping by XEDS were carried out using a JEOL 2100 F microscope
483 operating at 200 kV. This machine was equipped with a Schottky emission gun and an ultra-high-
484 resolution pole piece. HRTEM images were obtained with a Gatan US 4000 charge-coupled-device
485 (CCD) camera.

486 **Cryo soft X-ray tomography (cryo-SXT).** Imaging was conducted at ALBA synchrotron using cryo
487 transmission X-ray microscopy at Mistral beamline (Barcelona, Spain) (63) under the awarded proposals
488 2018022677 and 2019023346. Using a similar approach to that described above, MHB samples were
489 magnetically concentrated on the wall of an environmental sample bottle and then extracted by
490 micropipette. 5 µL of the magnetically concentrated MHB extract along with 1 µL of 100 nm Au
491 nanoparticles (BBI Solutions concentrated 5X) were added to a poly-l-lysine coated transmission electron
492 microscopy grids (Quantafoil R2/2 holey carbon, gold). Gold nanoparticles of 100 nm deposited on the
493 grid served as fiducial markers for projection alignment prior to tomographic reconstruction. The grid was
494 incubated horizontally for 1-2 min to allow deposition of MHB on the grid. The grid was then vertically
495 loaded into a Leica EM GP plunge freezer at 95 % humidity, blotted from the back of the grid with filter
496 paper (3 s blotting time) and then quickly dropped into a liquid ethane container (-180 ºC) cooled by
497 liquid nitrogen. Vitrified cells were kept under cryogenic conditions until being transferred to the
498 MISTRAL beamline cryo chamber for measurement. Tomograms of two MHB were collected.

499 A tilt series of projections from -65 ° to +65 ° was collected every 1 ° with an incident X-ray
500 energy of 520 eV. Exposure time varied from 1-2 s for each projection (2 s at higher angles). The sample
501 was imaged at 0 ° before and after collecting the tilt series to ensure there was no significant beam
502 damage at the achievable resolution. A 40 nm Fresnel zone plate was used with an effective pixel size of
503 12 nm. The projections were normalized with the incoming flux and deconvolved with the measured point
504 spread function (PSF) of the optical system (64). Alignment of projections was done with Etomo using
505 Au fiducials of 100 nm. Tomographic reconstruction and SIRT deconvolution were performed using
506 IMOD. Volume segmentation and visualization of tomograms was conducted using Microscopy Image
507 Browser (65) and Amira (FEI, USA) (66). Although this approach conserves the organization of MHB
508 cells in their native-state configuration, partial detachment of ectosymbionts was observed. However, the
509 majority of bacteria and their overall organization at the surface of their host were maintained.

510 **Scanning transmission X-ray microscopy (STXM) and X-ray magnetic circular dichroism (XMCD).**
511 Magnetotactic holobionts were magnetically concentrated using a low intensity magnet (~10 mT) for a
512 maximum time of 30 min to avoid remagnetization or any magnetic disturbance/interference with
513 magnetosomes. Cells were then transferred onto a light microscopy slide and magnetically transferred in a

514 clean drop of filtered environmental seawater. Cells aggregated at the edge of the filtered drop were then
515 micromanipulated with an InjectMan® NI2 micromanipulator and a CellTram® vario, hydraulic, manual
516 microinjector from Eppendorf mounted to a Leica DM IL LED microscope and further transferred in a
517 drop of fixative buffer containing 2.5 % (w/v) glutaraldehyde in sodium cacodylate buffer (0.1 M, pH 7.4)
518 prepared in filtered environmental seawater. Fixation occurred for only 10 seconds at room temperature
519 before the transfer of the cells, using the micromanipulator, onto a TEM copper grid coated with a carbon
520 film. A quick fixation was sufficient to conserve the ultrastructure of the holobiont and allow observation
521 of the biont's magnetosomes in the TEM. After their preparation, TEM grids were observed with STXM
522 without previous TEM analysis to avoid magnetic disturbance.

523 STXM-XMCD measurements were performed at HERMES, the soft X-ray spectromicroscopy
524 beamline at SOLEIL synchrotron (St. Aubin, France) (67, 68). A 25 nm Fresnel zone plate was employed
525 with measurements conducted under vacuum conditions at room temperature. Most STXM maps of MHB
526 were collected at 710 eV (at the Fe L_3-edge). Circularly polarized right (CPR) and left (CPL) light was
527 used without applied magnetic field to conserve the native-state magnetic moment of magnetosomes. To
528 retrieve an XMCD signal without applied fields, the sample was tilted 30 ° relative to the focal plane to
529 measure the intrinsic magnetic dipole moments of magnetosomes (38). XMCD maps were then generated
530 from the difference of OD-converted CPR and CPL images at 708.8 eV, the energy at which the strongest
531 XMCD signal was found. Other energies corresponded to 709.9 and 711.0 eV. Axis2000 and IgorPro
532 software were used to perform image work-up, analyses and create XMCD maps. XMCD maps were
533 obtained for at least five MEB of each of the three MHB measured.

534 **Micromagnetic simulations and calculations.** To determine the decay of the stray field from a straight
535 chain of 25 magnetosomes, we use a non-interacting point dipole approximation. Each point dipole is
536 taken to represent the center of a rhomboidal dodecahedron magnetosome with mid-sphere diameter of 60
537 nm (volume of 7.0×10^{-23} m^3), which, with a magnetite saturation magnetization of 4.8×10^5 $A \cdot m^{-1}$,
538 equates to a uniformly magnetized magnetosome moment of 3.36×10^{-17} $A \cdot m^2$ (total chain moment of
539 8.40×10^{-16} $A \cdot m^2$; 0.84 $fA \cdot m^2$). The magnetosome neighbor-to-neighbor edge separation is taken to be 10
540 nm. The net stray field is calculated as the sum of 25 magnetosome dipole fields at given distances
541 parallel and perpendicular to the chain axis (Fig. S7).

542 Micromagnetic models were used to determine the effect of curved chains around the host cell.
543 Magnetosome size, shape, and neighbor-to-neighbor edge separation are the same as described above.
544 The magnetosome chains were arranged in an arc defined by a circle of a specified radius, while
545 maintaining the face centered neighbor-to-neighbor edge separation of 10 nm. Mesh inputs were

546 generated using Trelis v17.1. The micromagnetic calculations were performed using MERRILL v1.6.4
547 (37). An example of a micromagnetic solution is shown in Fig. S8.

548 For a population of cells, the average alignment, <cosθ>, is dependent on the balance of magnetic
549 energy rotating the cell towards the magnetic field and thermal energy of randomizing Brownian rotation.
550 This can be expressed as:

$$\langle \cos\theta \rangle = L\left(\frac{mB}{k_B T}\right)$$

551 where m is the net moment of each cell, B is the magnetic field intensity, T is the temperature, k_B is the
552 Boltzmann constant, and $L(x) = \coth x - {}^{1}\!/_{x}$, is the Langevin function. A magnetotactic advantage will
553 be conferred to a population of cells if there is a net average bias of alignment of cells towards the
554 magnetic field direction where <cosθ> ≥ 0.5. Over the past 10,000 years in the Mediterranean region, the
555 field strength is consistently above 30 μT, which, at 20 °C, equates to a minimum moment per cell of 0.24
556 fA·m^2. For an extremely weak field of 3 μT, a minimum moment per cell of 2.4 fA·m^2 is required to
557 overcome Brownian motion and can be achieved with as few as two chains of magnetosomes (Fig. S8).

558

559 **Acknowledgements**

560 This work was supported by a grant from the CNRS – mission pour les initiatives transverses et
561 interdisciplinaires (MITI), adaptation du vivant à son environnement, projet *SymbioAdapt* and a project
562 from the French National Research Agency (ANR SymbioMagnet-21-CE02-0034-01). Romain Bolzoni
563 PhD contract was supported by the CNRS – MITI. D.M.C. acknowledges research funding through a
564 European Union Marie-Skłodowska Curie Action International Fellowship (MSCA-IF Project 797431:
565 BioNanoMagnets). D.M.C. and D.F. acknowledge awarded ALBA synchrotron beamtimes (Proposals
566 2018022677 and 2019023346), Mistral beamline staff for assistance in cryo-SXT experiments and
567 CALIPSO funding for Proposal 2019023346. We acknowledge Soleil Synchrotron for beamtime awarded
568 (Proposal 20191124) for experiments on the Hermes beamline (STXM-XMCD). W.W. would like to
569 acknowledge support from the Natural Environmental Research Council (NERC) through grants
570 NE/V001233/1 and NE/S011978/1. We thank Suri for his help in ultrathin-sections preparation. We thank
571 Jean-Michel Guigner for managing the TEM facility at IMPMC. G.A.P. is funded by a Natural
572 Environment Research Council Independent Research Fellowship (NE/P017266/1).

573

574 **References**

575 1. J.-B. Raina, *et al.*, Symbiosis in the microbial world: from ecology to genome evolution. *Biol. Open*
576 **7**, bio032524 (2018).

577 2. L. Margulis, R. Fester, *Symbiosis as a Source of Evolutionary Innovation: Speciation and*
578 *Morphogenesis* (MIT Press, 1991).

579 3. P. Lopez-Garcia, D. Moreira, The Syntrophy hypothesis for the origin of eukaryotes revisited. *Nat.*
580 *Microbiol.* **5**, 655–667 (2020).

581 4. P. López-García, L. Eme, D. Moreira, Symbiosis in eukaryotic evolution. *J. Theor. Biol.* **434**, 20–33
582 (2017).

583 5. P. Engel, N. A. Moran, The gut microbiota of insects - diversity in structure and function. *Fems*
584 *Microbiol. Rev.* **37**, 699–735 (2013).

585 6. P. Vandenkoornhuyse, A. Quaiser, M. Duhamel, A. Le Van, A. Dufresne, The importance of the
586 microbiome of the plant holobiont. *New Phytol.* **206**, 1196–1206 (2015).

587 7. T. Woyke, *et al.*, Symbiosis insights through metagenomic analysis of a microbial consortium.
588 *Nature* **443**, 950–955 (2006).

589 8. C. E. Harper, C. J. Hernandez, Cell biomechanics and mechanobiology in bacteria: Challenges and
590 opportunities. *APL Bioeng.* **4**, 021501 (2020).

591 9. J. Decelle, *et al.*, Subcellular architecture and metabolic connection in the planktonic
592 photosymbiosis between Collodaria (radiolarians) and their microalgae. *Environ. Microbiol.* **23**,
593 6569–6586 (2021).

594 10. J.-C. Simon, J. R. Marchesi, C. Mougel, M.-A. Selosse, Host-microbiota interactions: from
595 holobiont theory to analysis. *Microbiome* **7**, 5 (2019).

596 11. D. Faure, J.-C. Simon, T. Heulin, Holobiont: a conceptual framework to explore the eco-
597 evolutionary and functional implications of host-microbiota interactions in all ecosystems. *New*
598 *Phytol.* **218**, 1321–1324 (2018).

599 12. P. López-García, D. Moreira, Open questions on the origin of eukaryotes. *Trends Ecol. Evol.* **30**,
600 697–708 (2015).

601 13. M. Müller, *et al.*, Biochemistry and evolution of anaerobic energy metabolism in eukaryotes.
602 *Microbiol. Mol. Biol. Rev. MMBR* **76**, 444–495 (2012).

603 14. E. Hamann, *et al.*, Environmental Breviatea harbor mutualistic Arcobacter epibionts. *Nature* **534**,
604 254–258 (2016).

605 15. T. Vicsek, A. Zafeiris, Collective motion. *Phys. Rep.* **517**, 71–140 (2012).

606 16. A. M. Wier, *et al.*, Spirochete attachment ultrastructure: Implications for the origin and evolution of
607 cilia. *Biol. Bull.* **218**, 25–35 (2010).

608 17. C. L. Monteil, *et al.*, A symbiotic origin of magnetoreception in unicellular eukaryotes. *Nat.*
609 *Microbiol.* **4**, 1088–1095 (2019).

610 18. D. A. Bazylinski, R. B. Frankel, Magnetosome formation in prokaryotes. *Nat. Rev. Microbiol.* **2**,
611 217–230 (2004).

612 19. C. T. Lefèvre, *et al.*, Diversity of magneto-aerotactic behaviors and oxygen sensing mechanisms in
613 cultured magnetotactic bacteria. *Biophys. J.* **107**, 527–538 (2014).

614 20. X. Mao, R. Egli, X. Liu, L. Zhao, Magnetotactic advantage in stable sediment by long-term
615 observations of magnetotactic bacteria in Earth's field, zero field and alternating field. *PloS One* **17**,
616 e0263593 (2022).

617 21. X.-X. Qian, *et al.*, Juxtaposed membranes underpin cellular adhesion and display unilateral cell
618 division of multicellular magnetotactic prokaryotes. *Environ. Microbiol.* **22**, 1481–1494 (2020).

619 22. D. Pfeiffer, *et al.*, A bacterial cytolinker couples positioning of magnetic organelles to cell shape
620 control. *Proc. Natl. Acad. Sci. U. S. A.* **117**, 32086–32097 (2020).

621 23. M. Toro-Nahuelpan, *et al.*, MamY is a membrane-bound protein that aligns magnetosomes and the
622 motility axis of helical magnetotactic bacteria. *Nat. Microbiol.* **4**, 1978–1989 (2019).

623 24. C. T. Lefèvre, M. Bennet, S. Klumpp, D. Faivre, Positioning the Flagellum at the Center of a
624 Dividing Cell To Combine Bacterial Division with Magnetic Polarity. *mBio* **6**, e02286 (2015).

625 25. M. Toro-Nahuelpan, *et al.*, Segregation of prokaryotic magnetosomes organelles is driven by
626 treadmilling of a dynamic actin-like MamK filament. *BMC Biol.* **14**, 88 (2016).

627 26. M. L. Ginger, N. Portman, P. G. McKean, Swimming with protists: perception, motility and
628 flagellum assembly. *Nat. Rev. Microbiol.* **6**, 838–850 (2008).

629 27. D. Esquivel, H. Debarros, M. Farina, P. Aragao, J. Danon, Magnetotactic Microorganisms in the
630 Rio-De-Janeiro Region. *Biol. Cell* **47**, 227–233 (1983).

631 28. M. Perantoni, *et al.*, Magnetic properties of the microorganism Candidatus Magnetoglobus
632 multicellularis. *Naturwissenschaften* **96**, 685–690 (2009).

633 29. F. F. T. de Araujo, M. A. Pires, R. B. Frankel, C. E. M. Bicudo, Magnetite and Magnetotaxis in
634 Algae. *Biophys. J.* **50**, 375–378 (1986).

635 30. P. Leão, *et al.*, Magnetosome magnetite biomineralization in a flagellated protist: evidence for an
636 early evolutionary origin for magnetoreception in eukaryotes? *Environ. Microbiol.* **22**, 1495–1506
637 (2019).

638 31. M. P. Pichel, T. A. G. Hageman, I. S. M. Khalil, A. Manz, L. Abelmann, Magnetic response of
639 Magnetospirillum gryphiswaldense observed inside a microfluidic channel. *J. Magn. Magn. Mater.*
640 **460**, 340–353 (2018).

641 32. C. Zahn, *et al.*, Measurement of the magnetic moment of single Magnetospirillum gryphiswaldense
642 cells by magnetic tweezers. *Sci. Rep.* **7**, 1–14 (2017).

643 33. R. Nadkarni, S. Barkley, C. Fradin, A comparison of methods to measure the magnetic moment of
644 magnetotactic bacteria through analysis of their trajectories in external magnetic fields. *PLoS ONE*
645 **8**, e82064 (2013).

646 34. R. E. Dunin-Borkowski, *et al.*, Magnetic microstructure of magnetotactic bacteria by electron
647 holography. *Science* **282**, 1868–1870 (1998).

648 35. F. Abreu, *et al.*, Cell adhesion, multicellular morphology, and magnetosome distribution in the
649 multicellular magnetotactic prokaryote Candidatus Magnetoglobus multicellularis. *Microsc.*
650 *Microanal. Off. J. Microsc. Soc. Am. Microbeam Anal. Soc. Microsc. Soc. Can.* **3**, 1–9 (2013).

651 36. P. Leão, *et al.*, Ultrastructure of ellipsoidal magnetotactic multicellular prokaryotes depicts their
652 complex assemblage and cellular polarity in the context of magnetotaxis. *Environ. Microbiol.* **19**,
653 2151–2163 (2017).

654 37. P. O. Conbhui, *et al.*, MERRILL: Micromagnetic Earth Related Robust Interpreted Language
655 Laboratory. *Geochem. Geophys. Geosystems* **19**, 1080–1106 (2018).

656 38. L. Le Nagard, *et al.*, Magnetite magnetosome biomineralization in Magnetospirillum magneticum
657 strain AMB-1: A time course study. *Chem. Geol.* **530**, 119348 (2019).

658 39. F. C. Meldrum, S. Mann, B. R. Heywood, R. B. Frankel, D. A. Bazylinski, Electron-microscopy
659 study of magnetosomes in a cultured coccoid magnetotactic bacterium. *Proc. R. Soc. Lond. Ser. B-*
660 *Biol. Sci.* **251**, 231–236 (1993).

661 40. F. C. Meldrum, S. Mann, B. R. Heywood, R. B. Frankel, D. A. Bazylinski, Electron-microscopy
662 study of magnetosomes in 2 cultured vibrioid magnetotactic bacteria. *Proc. R. Soc. Lond. Ser. B-*
663 *Biol. Sci.* **251**, 237–242 (1993).

664 41. M. Pósfai, C. T. Lefèvre, D. Trubitsyn, D. A. Bazylinski, R. B. Frankel, Phylogenetic significance
665 of composition and crystal morphology of magnetosome minerals. *Front. Microbiol.* **4**, 344 (2013).

666 42. M. Winklhofer, L. G. Abraçado, A. F. Davila, C. N. Keim, H. G. P. Lins de Barros, Magnetic
667 optimization in a multicellular magnetotactic organism. *Biophys. J.* **92**, 661–670 (2007).

668 43. C. T. Lefèvre, *et al.*, Monophyletic origin of magnetotaxis and the first magnetosomes. *Environ.*
669 *Microbiol.* **15**, 2267–2274 (2013).

670 44. E. C. T. Descamps, J.-B. Abbé, D. Pignol, C. T. Lefèvre, "Controlled Biomineralization of
671 Magnetite in Bacteria" in *Iron Oxides*, D. Faivre, Ed. (Wiley-VCH Verlag GmbH & Co. KGaA,
672 2016), pp. 99–116.

673 45. R. B. Frankel, R. P. Blakemore, Navigational compass in magnetic bacteria. *J. Magn. Magn. Mater.*
674 **15–8**, 1562–1564 (1980).

675 46. D. M. S. Esquivel, H. G. P. Lins De Barros, Motion of Magnetotactic Microorganisms. *J. Exp. Biol.*
676 **121**, 153–163 (1986).

677 47. N. Petersen, D. G. Weiss, H. Vali, "Magnetic bacteria in lake sediments" in *Geomagnetism and*
678 *Palaeomagnetism*, NATO ASI Series., F. J. Lowes, *et al.*, Eds. (Springer Netherlands, 1989), pp.
679 231–241.

680 48. Y. Pan, *et al.*, Reduced efficiency of magnetotaxis in magnetotactic coccoid bacteria in higher than
681 geomagnetic fields. *Biophys. J.* **97**, 986–991 (2009).

682 49. E. Wajnberg, L. Desouza, H. Debarros, D. Esquivel, A Study of Magnetic-Properties of
683 Magnetotactic Bacteria. *Biophys. J.* **50**, 451–455 (1986).

684 50. S. S. Kalirai, D. A. Bazylinski, A. P. Hitchcock, Anomalous magnetic orientations of magnetosome
685 chains in a magnetotactic bacterium: Magnetovibrio blakemorei strain MV-1. *PloS One* **8**, e53368
686 (2013).

687 51. E. F. DeLong, R. B. Frankel, D. A. Bazylinski, Multiple evolutionary origins of magnetotaxis in
688 bacteria. *Science* **259**, 803–806 (1993).

689 52. W. Lin, *et al.*, Origin of microbial biomineralization and magnetotaxis during the Archean. *Proc.*
690 *Natl. Acad. Sci. U. S. A.* **114**, 2171–2176 (2017).

691 53. J. M. Byrne, *et al.*, Redox cycling of Fe(II) and Fe(III) in magnetite by Fe-metabolizing bacteria.
692 *Science* **347**, 1473–1476 (2015).

693 54. V. P. Edgcomb, *et al.*, Identity of epibiotic bacteria on symbiontid euglenozoans in O2-depleted
694 marine sediments: evidence for symbiont and host co-evolution. *ISME J.* **5**, 231–243 (2011).

695 55. F. F. Guo, *et al.*, Magnetosomes eliminate intracellular reactive oxygen species in Magnetospirillum
696 gryphiswaldense MSR-1. *Environ. Microbiol.* **14**, 1722–1729 (2012).

697 56. K. Li, *et al.*, Magnetosomes extracted from Magnetospirillum magneticum strain AMB-1 showed
698 enhanced peroxidase-like activity under visible-light irradiation. *Enzyme Microb. Technol.* **72**, 72–
699 78 (2015).

700 57. T. Fenchel, B. Finlay, Oxygen and the spatial structure of microbial communities. *Biol. Rev. Camb.*
701 *Philos. Soc.* **83**, 553–569 (2008).

702 58. D. Schüler, E. Baeuerlein, Dynamics of iron uptake and Fe3O4 biomineralization during aerobic
703 and microaerobic growth of Magnetospirillum gryphiswaldense. *J. Bacteriol.* **180**, 159–162 (1998).

704 59. R. B. Frankel, D. A. Bazylinski, M. S. Johnson, B. L. Taylor, Magneto-aerotaxis in marine coccoid
705 bacteria. *Biophys. J.* **73**, 994–1000 (1997).

706 60. N. Philippe, L.-F. Wu, An MCP-like protein interacts with the MamK cytoskeleton and is involved
707 in magnetotaxis in Magnetospirillum magneticum AMB-1. *J. Mol. Biol.* **400**, 309–322 (2010).

708 61. D. Schüler, The biomineralization of magnetosomes in Magnetospirillum gryphiswaldense. *Int.*
709 *Microbiol. Off. J. Span. Soc. Microbiol.* **5**, 209–214 (2002).

710 62. M. Bennet, *et al.*, Influence of Magnetic Fields on Magneto-Aerotaxis. *PLoS ONE* **9**, e101150
711 (2014).

712 63. A. Sorrentino, *et al.*, MISTRAL: a transmission soft X-ray microscopy beamline for cryo nano-
713 tomography of biological samples and magnetic domains imaging. *J. Synchrotron Radiat.* **22**, 1112–
714 1117 (2015).

715 64. J. Otón, *et al.*, Characterization of transfer function, resolution and depth of field of a soft X-ray
716 microscope applied to tomography enhancement by Wiener deconvolution. *Biomed. Opt. Express* **7**,
717 5092–5103 (2016).

718 65. I. Belevich, M. Joensuu, D. Kumar, H. Vihinen, E. Jokitalo, Microscopy Image Browser: A
719 Platform for Segmentation and Analysis of Multidimensional Datasets. *PLOS Biol.* **14**, e1002340
720 (2016).

721 66. D. Stalling, M. Westerhoff, H.-C. Hege, “38 - amira: A Highly Interactive System for Visual Data
722 Analysis” in *Visualization Handbook*, C. D. Hansen, C. R. Johnson, Eds. (Butterworth-Heinemann,
723 2005), pp. 749–767.

724 67. R. Belkhou, *et al.*, HERMES: a soft X-ray beamline dedicated to X-ray microscopy. *J. Synchrotron*
725 *Radiat.* **22**, 968–979 (2015).

726 68. S. Swaraj, *et al.*, Performance of the HERMES beamline at the carbon K-edge. *J. Phys. Conf. Ser.*
727 **849**, 012046 (2017).

728

729 **Figures legend**

730 **Fig. 1. Observation of the motility apparatus of MHBs isolated from Carry-le-Rouet, France.** (*A*-*C*)
731 SEM images of cells prepared using a critical-point drying approach showing (*A*) a whole MHB, (*B*) a
732 higher magnification of the same holobiont observed at 2 kV showing the surface of the holobiont, and
733 (*C*) the same as in (B) but observed at 10 kV using the backscattered mode showing the magnetosome
734 chains inside the ectosymbiotic bacteria. (*D*) Stitched TEM images of longitudinal ultrathin sections of a
735 MHB showing the vestibulum on the front of the protistan cells and the two flagella and (*E*) TEM image
736 showing one flagellum emerging from this cavity. Nu: nucleus; MEB: magnetic ectosymbiotic bacteria;
737 F: flagella; V: vestibulum.

738 **Fig. 2. Observation of the magnetic response of MHBs isolated from Carry-le-Rouet, France.** (*A*)
739 Optical microscopy image of a swimming MHB showing the position of the flagella. (*B*) Schematic of U-
740 turn trajectory measurements during magnetic field reversal. (*C*) The trajectory plot of a U-turn at 3.5 mT
741 magnetic field switching. The instantaneous velocity ($\mu m \cdot s^{-1}$) is represented in color indicating the MHB
742 motility direction where the blue color indicates upwards motion and red color the downward
743 displacement. (*D*) Time difference subtracted from first derivate peaks (t_1 and t_2) of the Y trajectory to
744 yield τ_{Uturn}.

745 **Fig. 3. 3-D reconstruction of vitrified MHB using cryo soft X-ray tomography (cryo-SXT).** (*A*)
746 Virtual slices of X-ray tomography reconstruction through the Z-direction from top to bottom of MHB
747 (see Movie S2). (*B*) Volume reconstruction of magnetosome chains (red), ectosymbiotic bacteria
748 membrane (yellow), the protistan host (cyan) and dense intracellular granules (white) from different
749 viewpoints.

Fig. 4. Organization and attachment of ectosymbiotic bacteria at the surface of their host. Transmission electron microscope images in bright field mode of ultrathin sections of MHB showing (*A,B*) the presence of only one layer of bacteria at the surface of their host, (*C*) the presence of bacteria in channels formed at the surface of their host, (*C,D*) the proximity of ectosymbionts with hydrogenosomes, (*C-E,* white arrows) the wing-like structures that are outgrowths of bacterial external membrane, and (*C-F,* black arrows) the presence of vesicles between the bacteria. Nu: nucleus; H: hydrogenosomes. All are transverse sections except for *F*, which is longitudinal.

Fig. 5. Magnetic moment orientation of magnetosomes relative to the protistan flagella using soft X-ray scanning transmission X-ray microscopy (STXM) at the Fe L-edge and X-ray magnetic circular dichroism (XMCD) without applied magnetic fields. (*A,B*) STXM images at 710 eV of MHB deposited in opposite directions. Fla: flagella; Dmg: X-ray beam damage from previous scans. Colored frames indicate the regions further analyzed. (*C,D*) Optical density maps (left-side panels) and difference maps of circular polarization left (CPL) and circular polarization right (CPR) at 708.8 eV (where maximum XMCD signal was found) (right-side panels).

Fig. 6. Crystallography of the cuboctahedral/prismatic magnetite particles produced by a magnetic ectosymbiotic bacteria. (*A*) Transmission electron microscope bright-field (TEM-BF) image of a magnetic ectosymbiotic bacterium detached from its host and its single magnetosome chain (*B*). (*C*) High-resolution transmission electron microscopy (HR-TEM) images of the crystals annotated 1-6 in (*B*). Prismatic models drawn in white were superimposed on the image of these crystals with an acceptable match. Yellow arrows indicate the <111> direction: plain arrows correspond to in plane direction and dashed arrows are related to out-of-plane direction (for the latter, smaller arrow length corresponds to a higher out-of-plane angle). (*D*) FFT pattern of these HR-TEM indexed with the magnetite structure (spacegroup $Fm\bar{3}m$, a = 8.04 Å). (*E*) Stereographic projection oriented with respect to the orientation inferred from (*D*) using SingleCrystal software. The orientations of the models and the <111> directions were deduced from the stereographic projections

A
2 µm

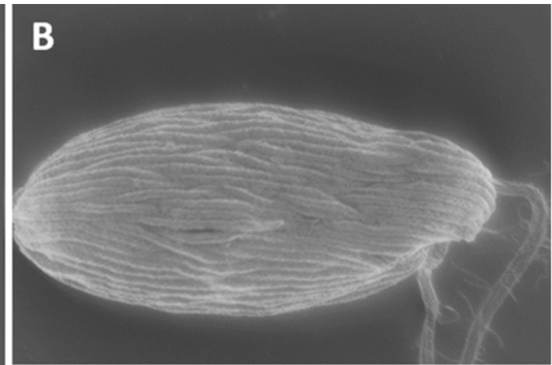
B

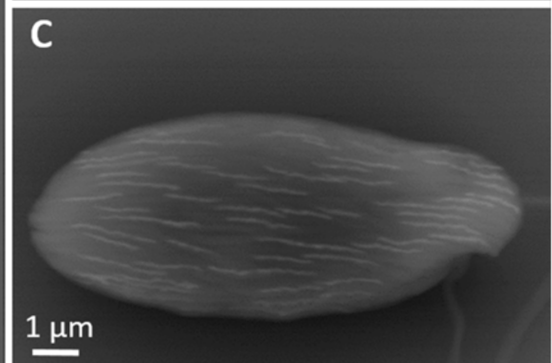
C
1 µm

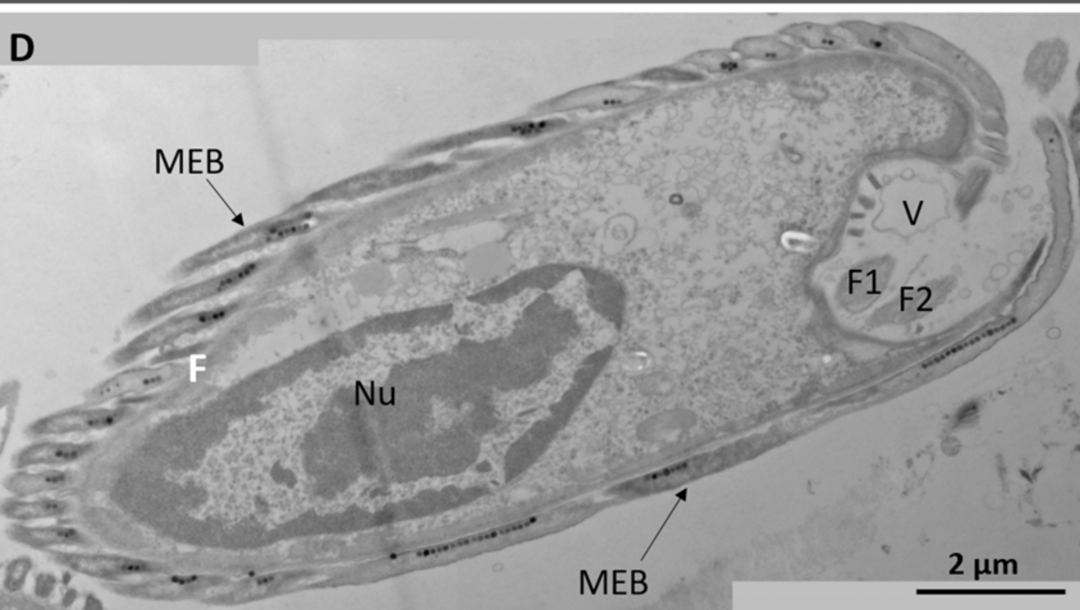
D
MEB
V
F1
F2
F
Nu
MEB
2 µm

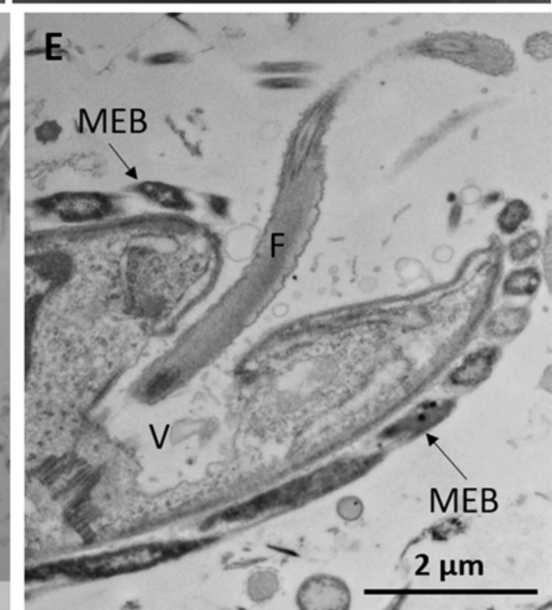
E
MEB
F
V
MEB
2 µm

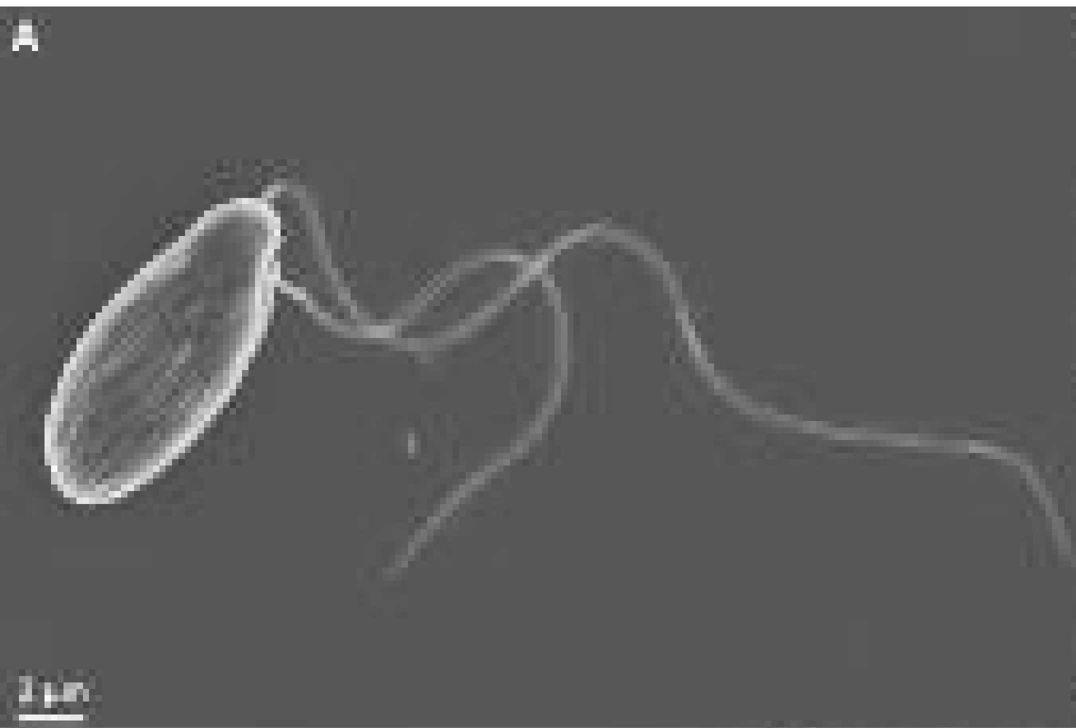
A

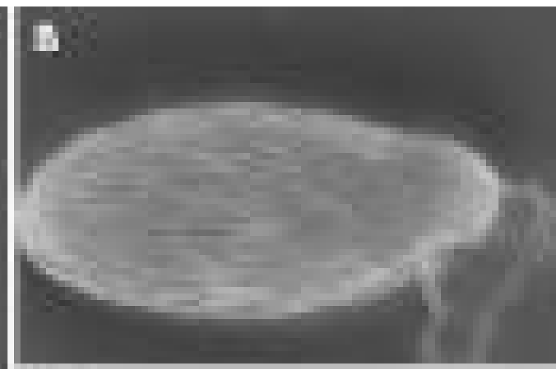
B

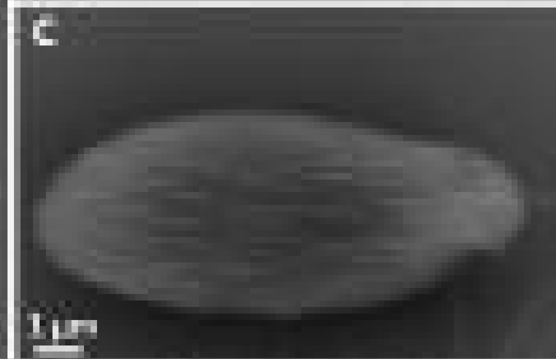
C

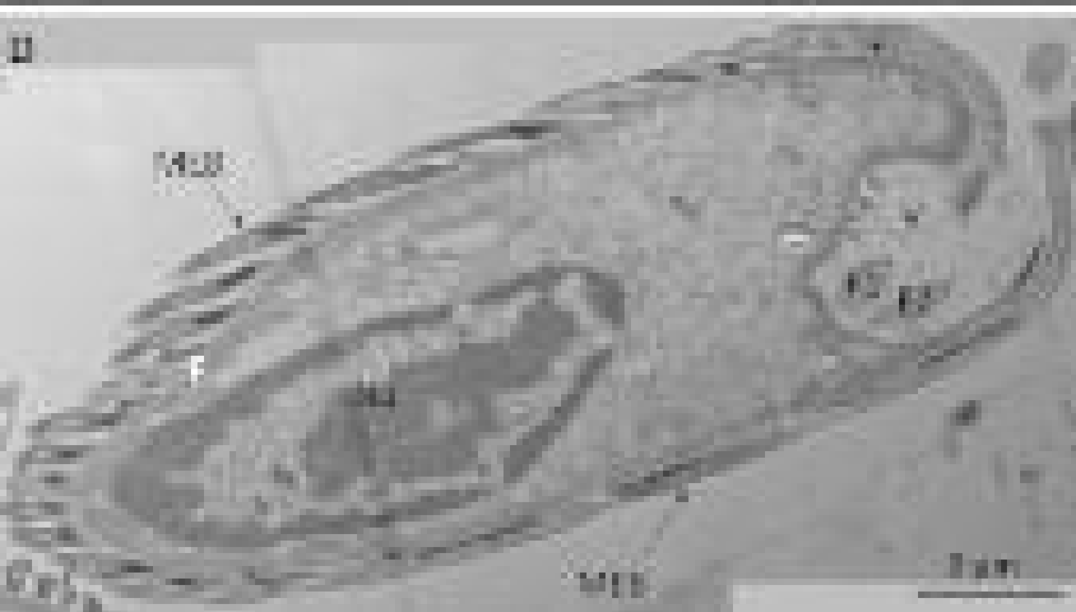

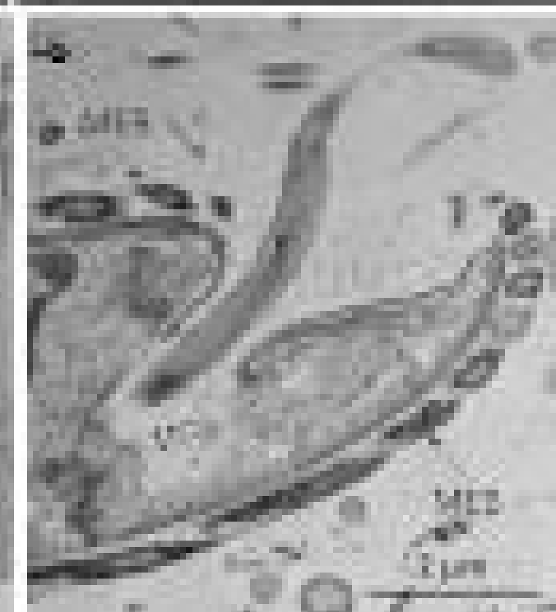

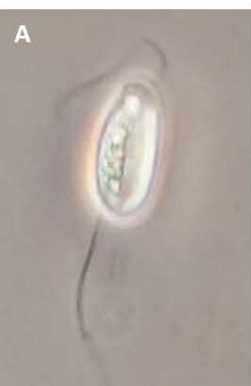
A

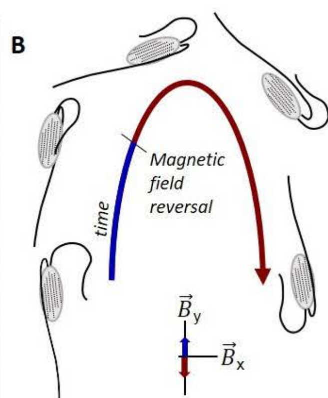
B
Magnetic field reversal
time
$\vec{B}_y$
$\vec{B}_x$

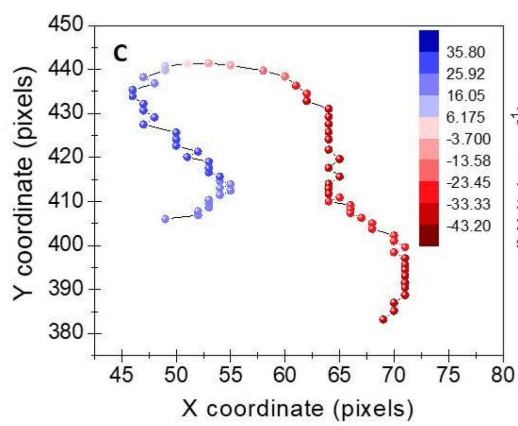
C
Y coordinate (pixels)
X coordinate (pixels)
35.80
25.92
16.05
6.175
-3.700
-13.58
-23.45
-33.33
-43.20

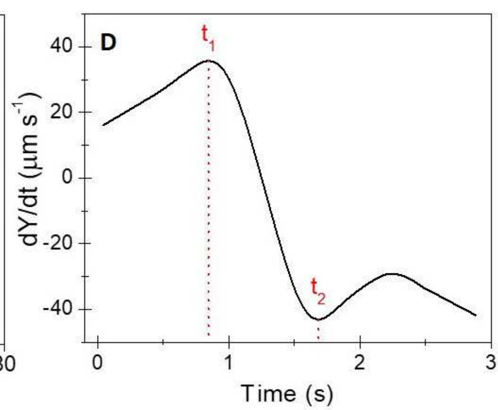
D
t_1
t_2
dY/dt (µm s^{-1})
Time (s)

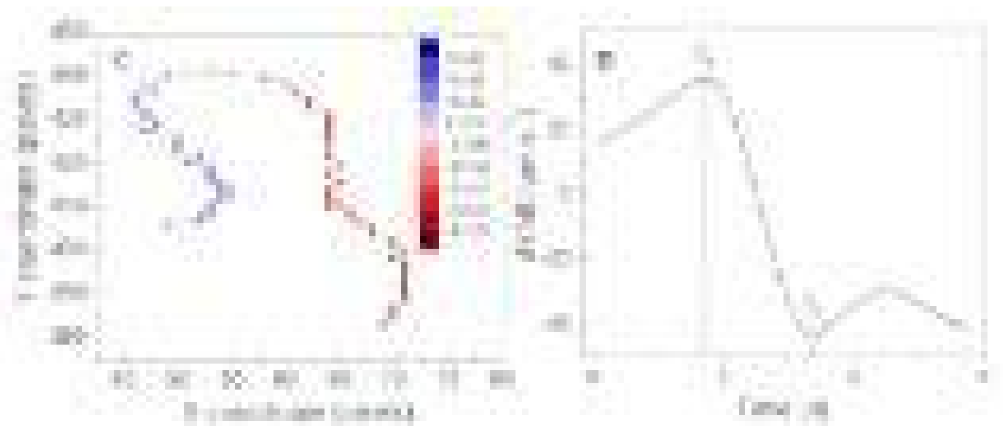

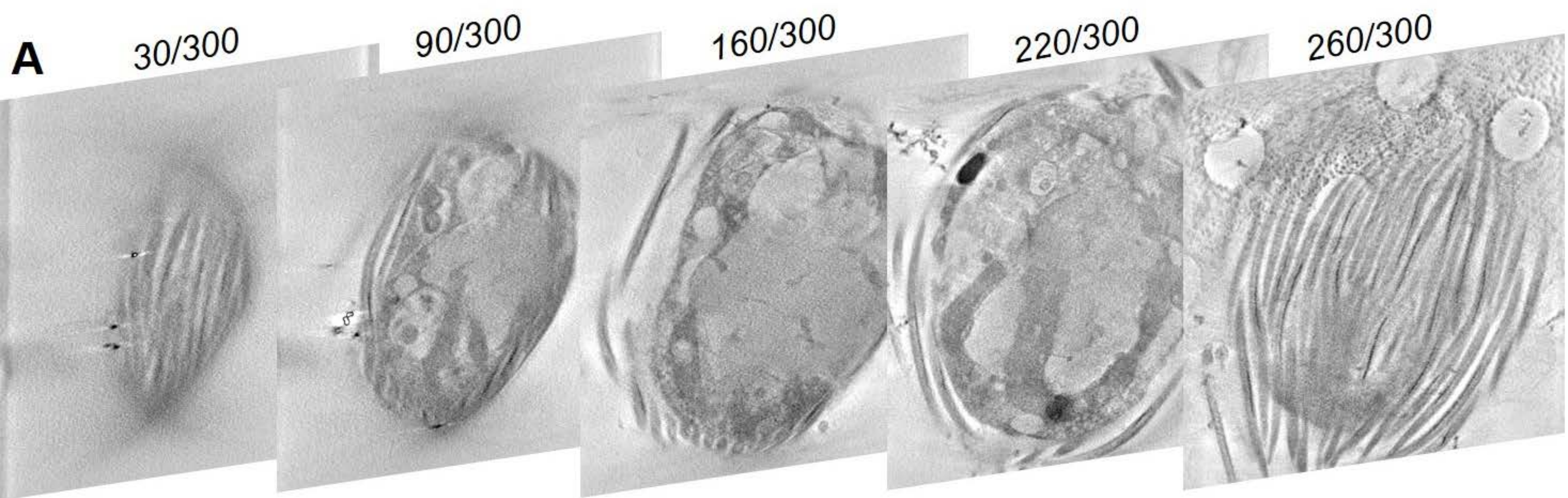
A
30/300
90/300
160/300
220/300
260/300

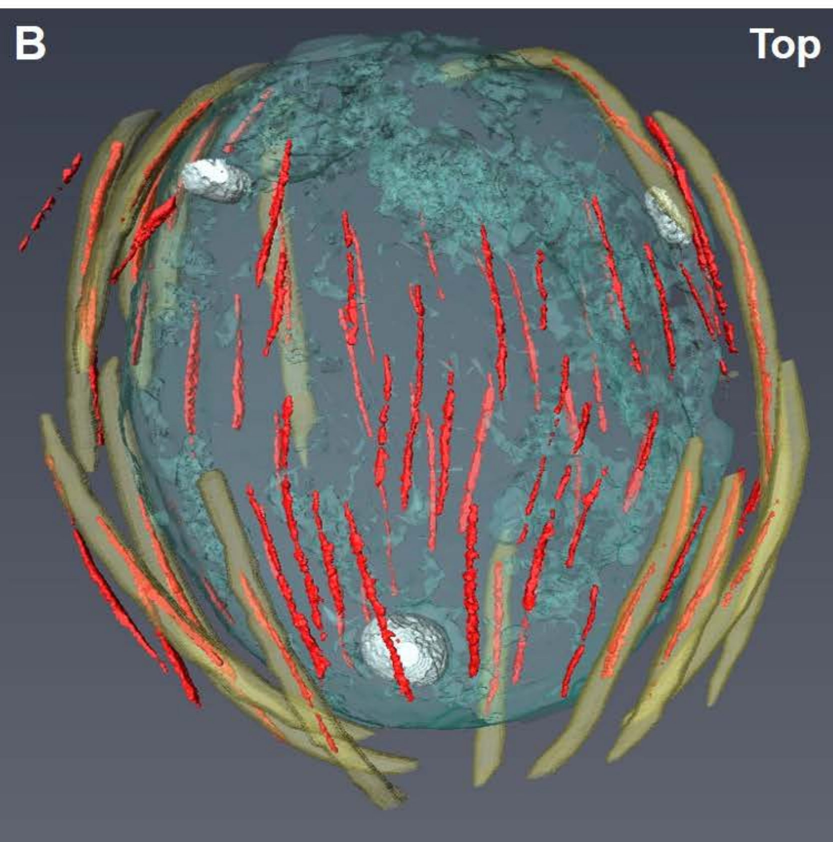
B
Top

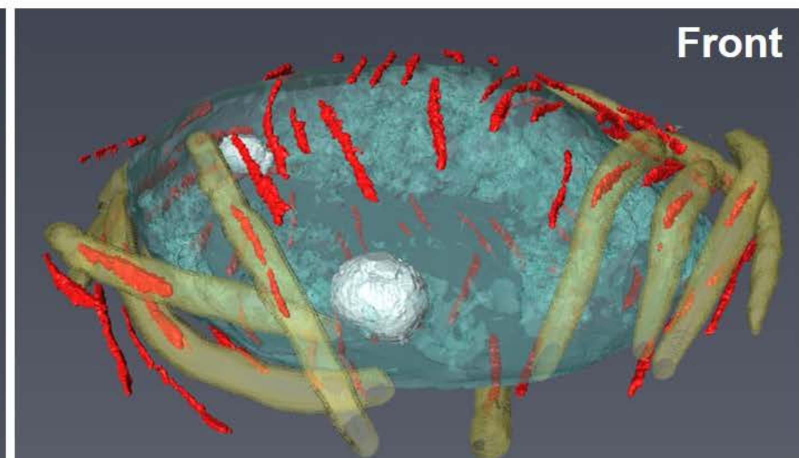
Front

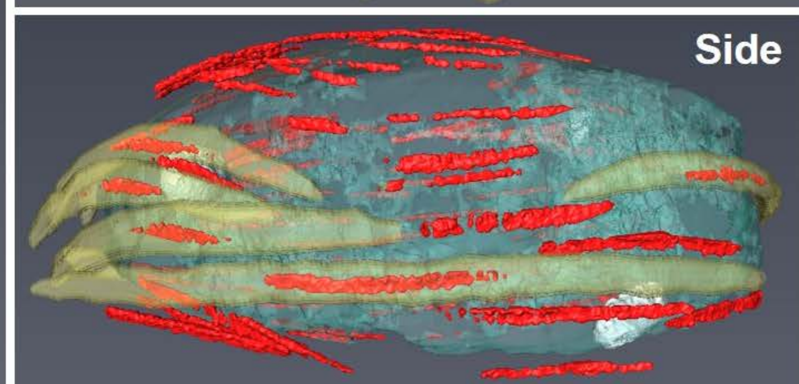
Side

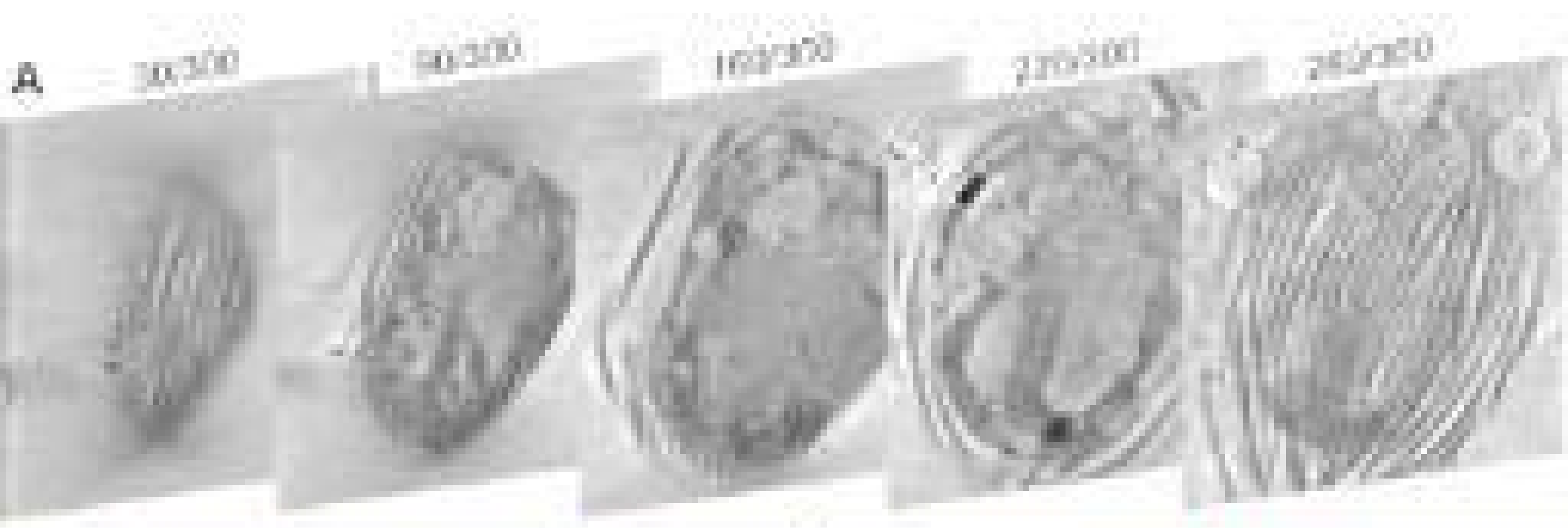
A
B
Top
Front
Side

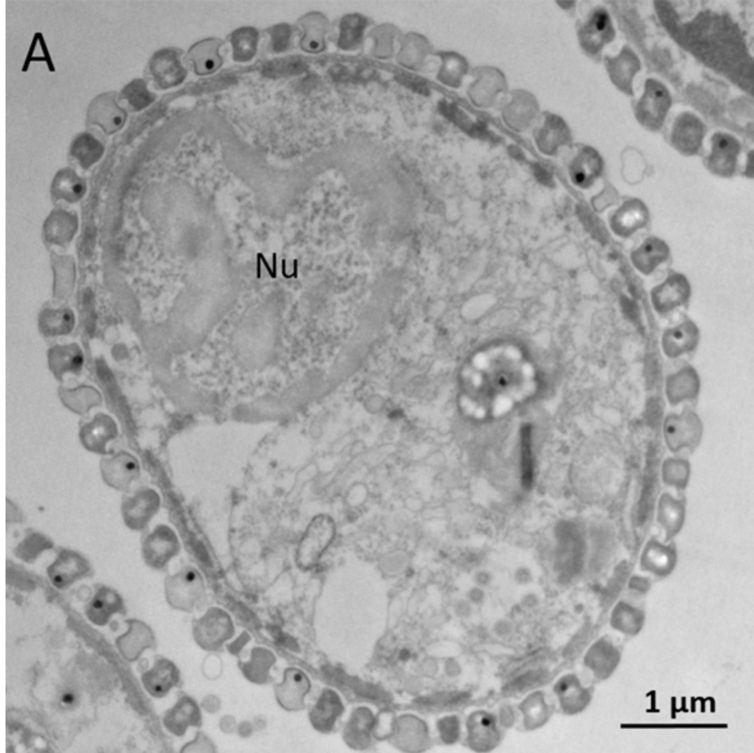
A
Nu
1 µm

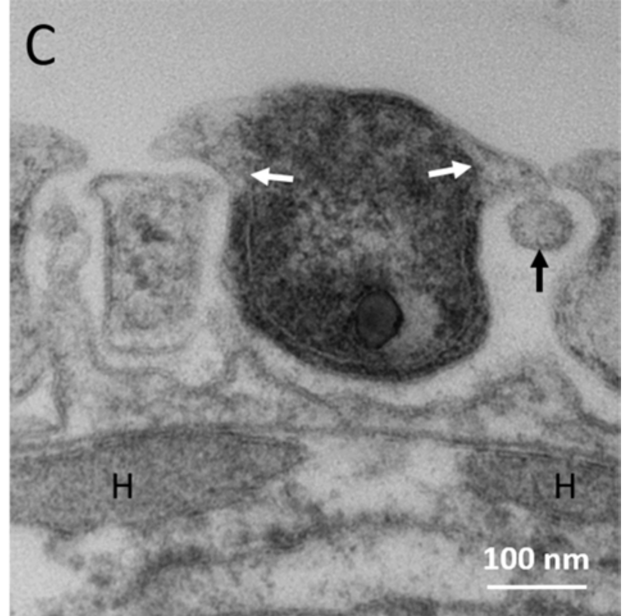
C
H
H
100 nm

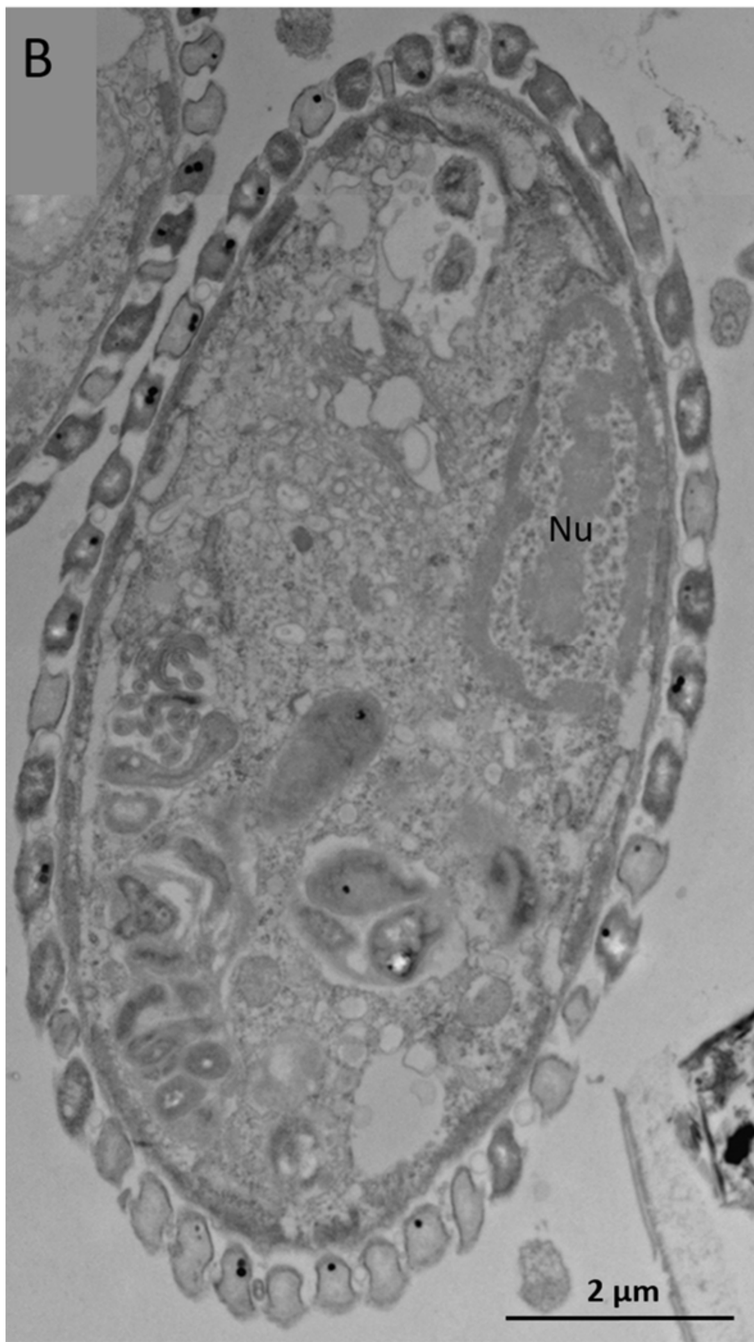
B
Nu
2 µm

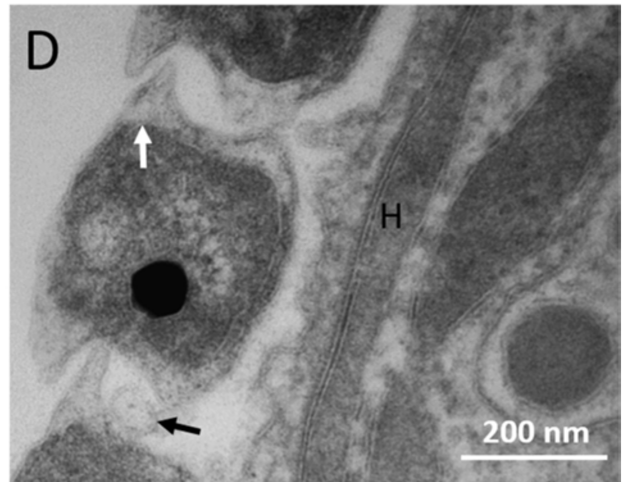
D
H
200 nm

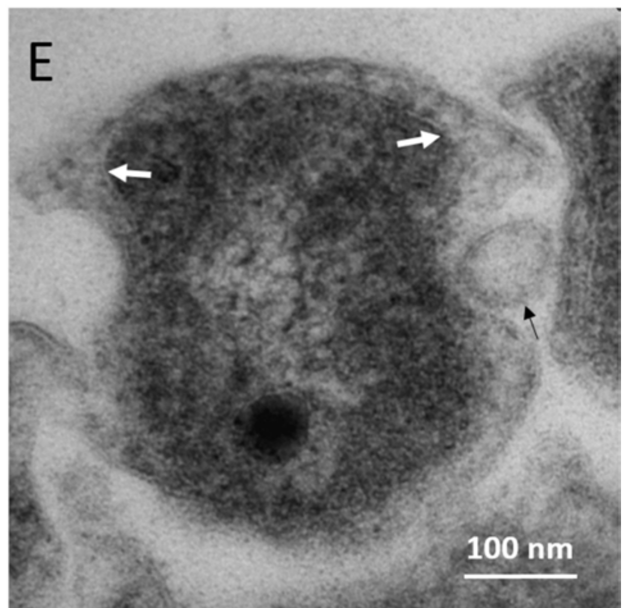
E
100 nm

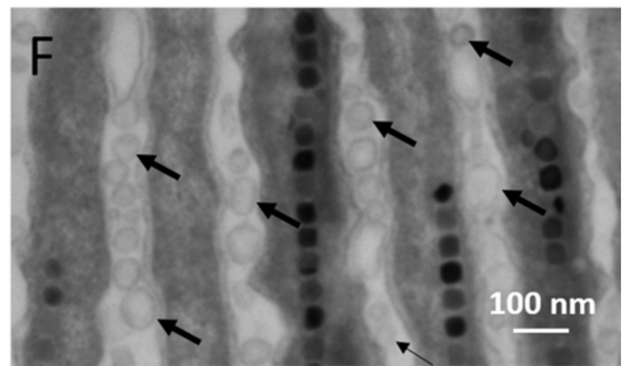
F
100 nm

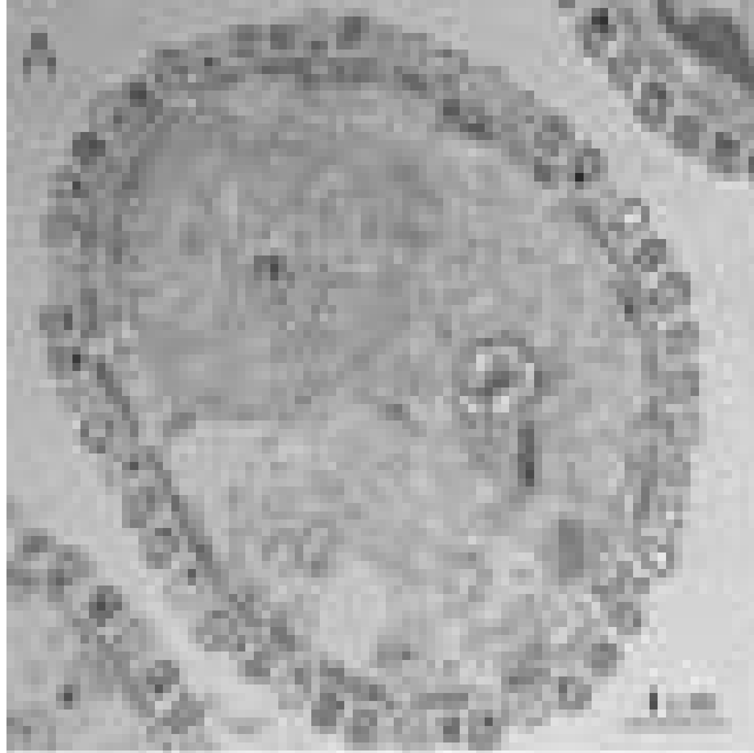

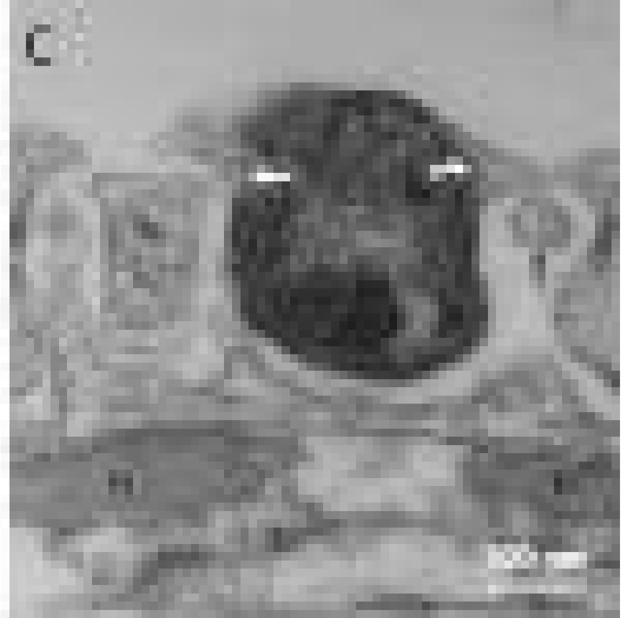

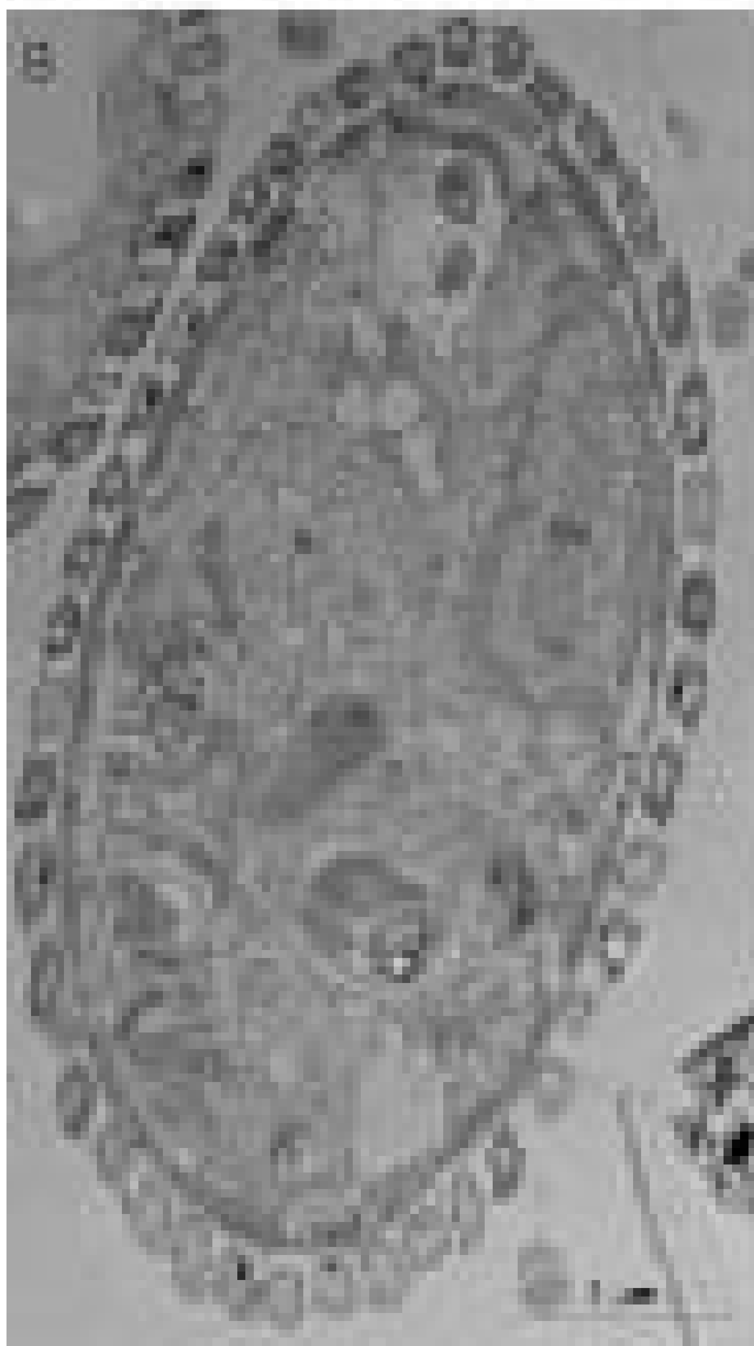

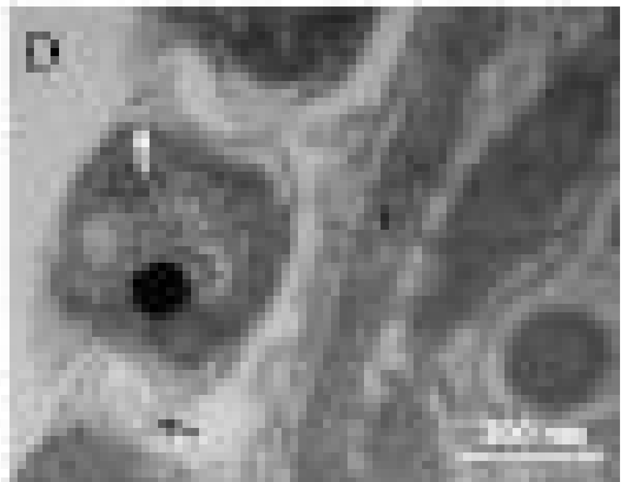

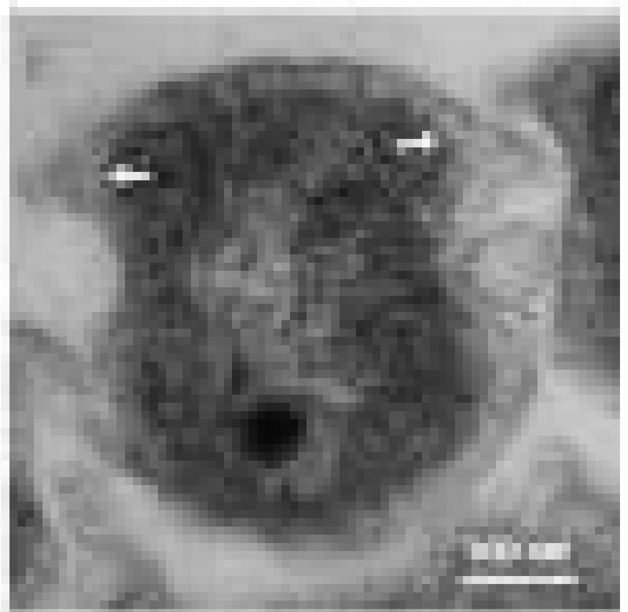

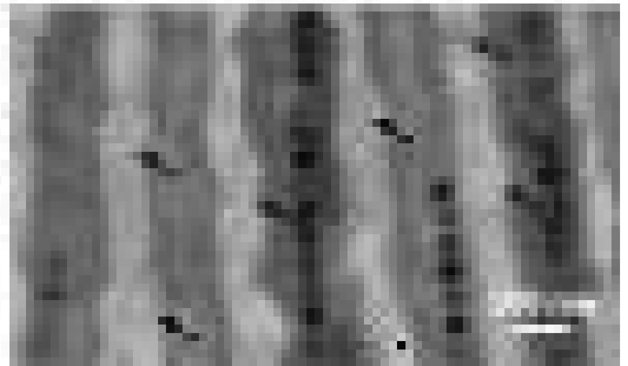

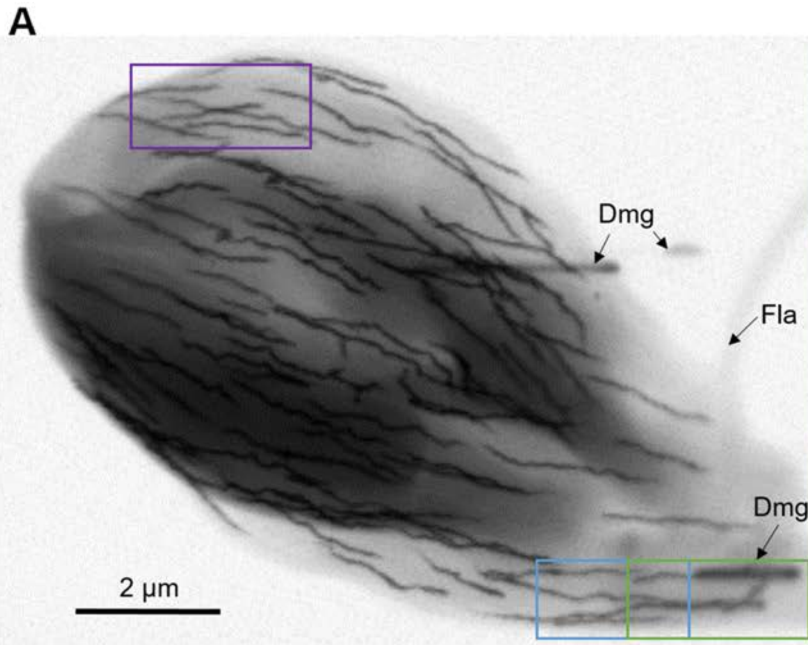
A
Dmg
Fla
Dmg
2 µm

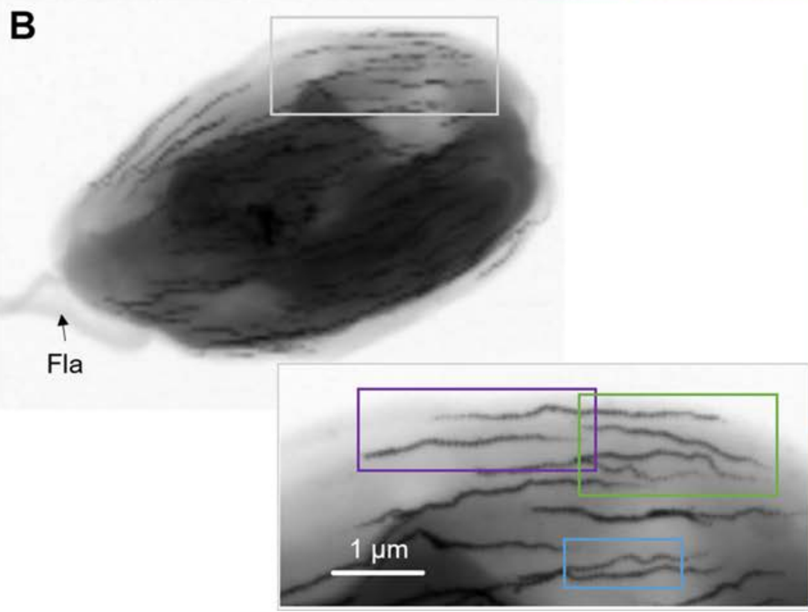
B
Fla
1 µm

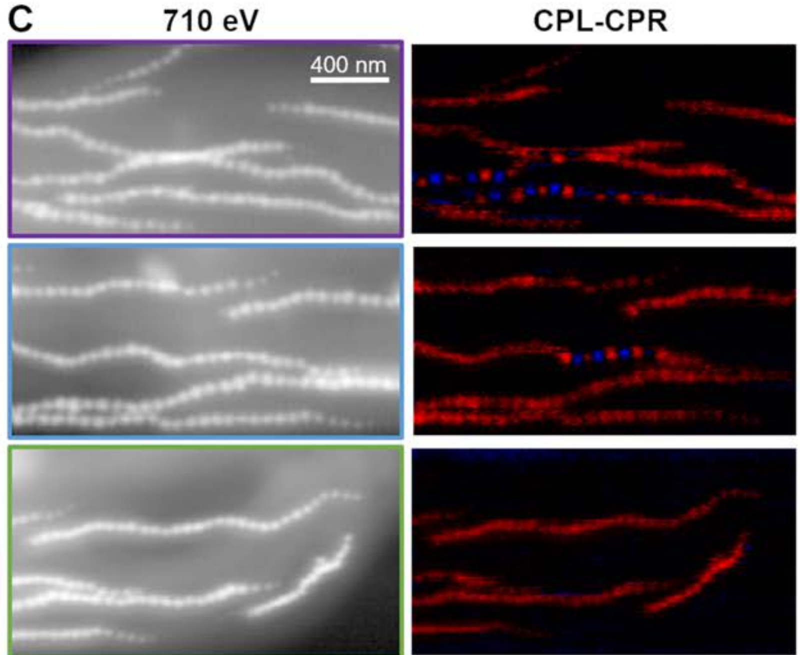
C
710 eV
CPL-CPR
400 nm

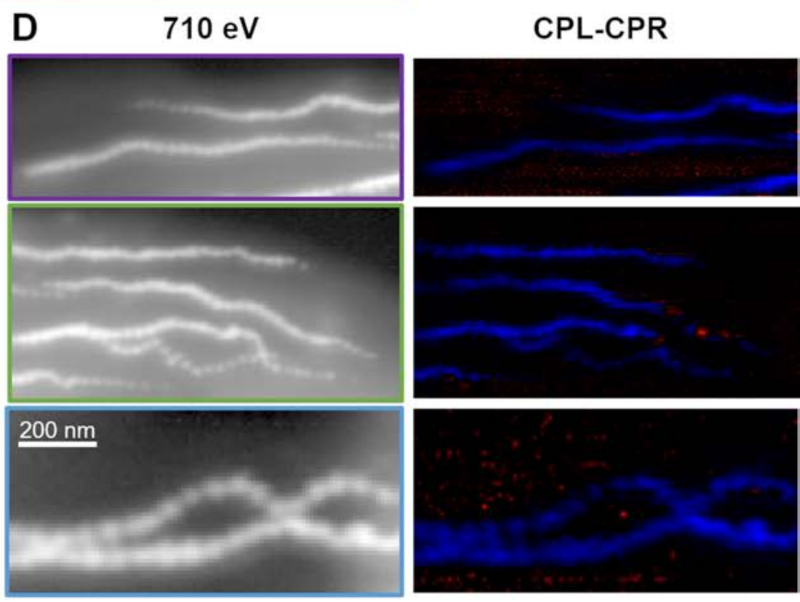
D
710 eV
CPL-CPR
200 nm

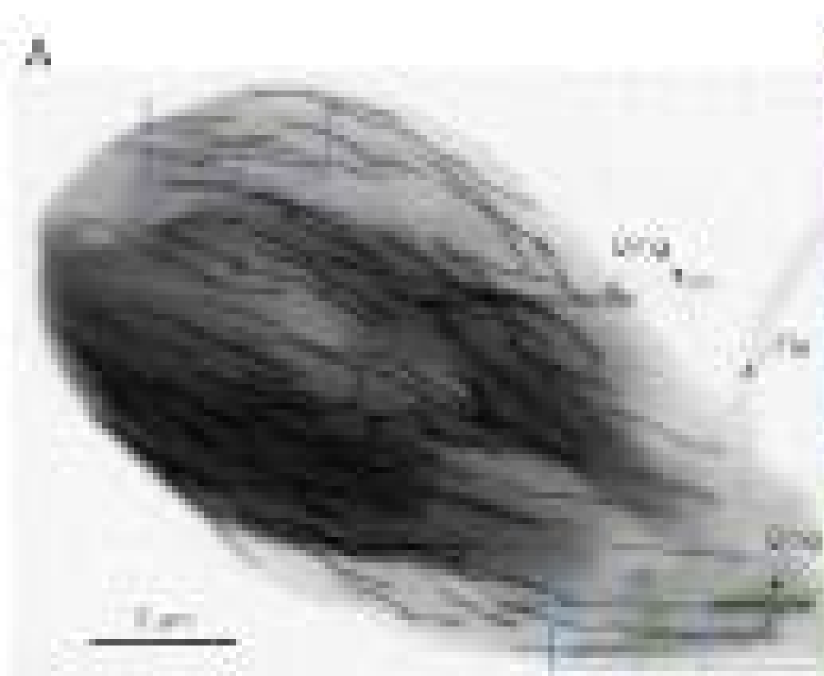
A

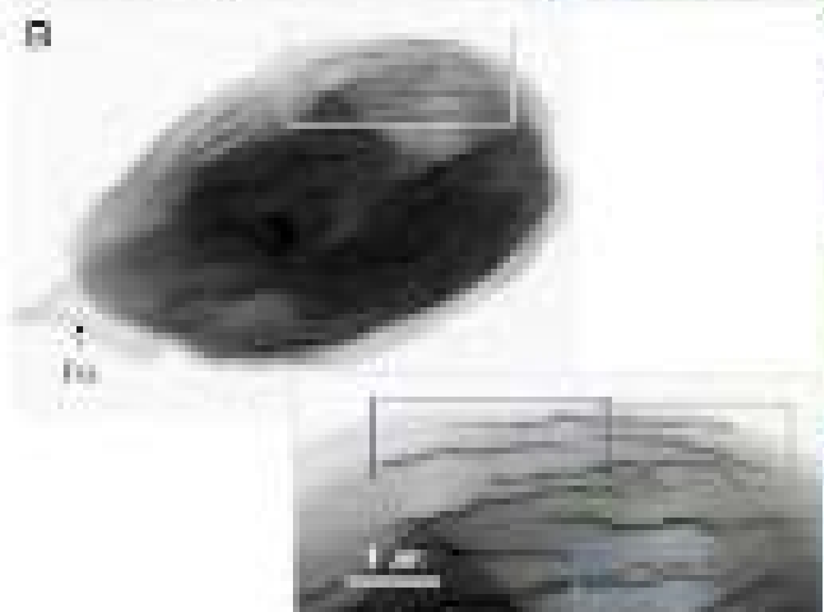
B

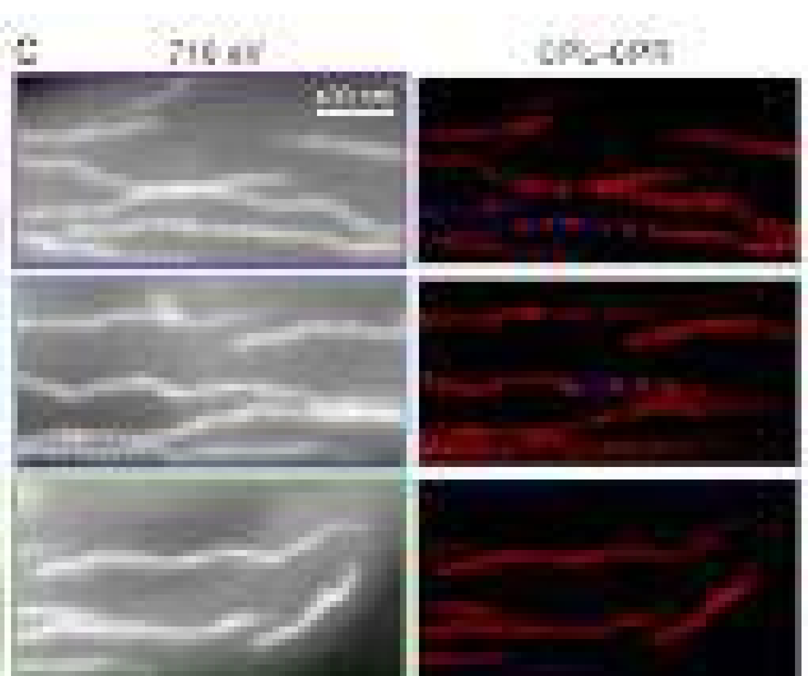
C

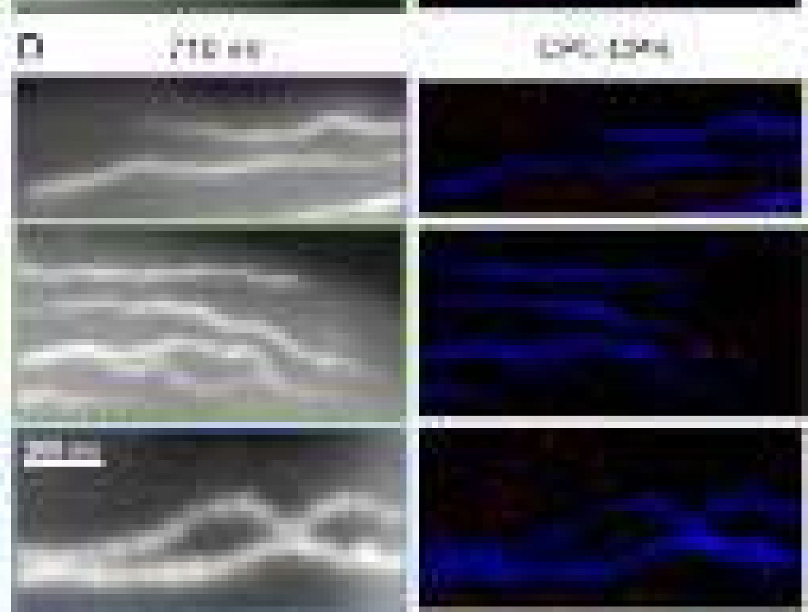
D

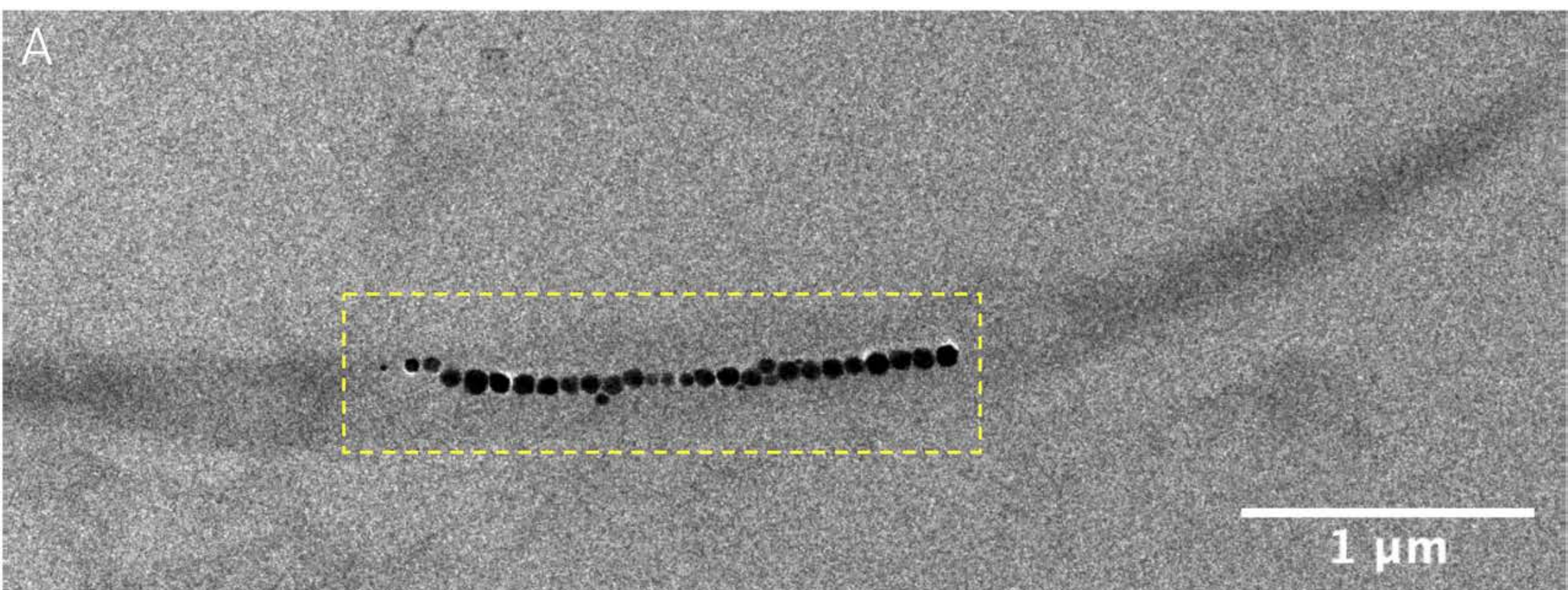
A
1 µm

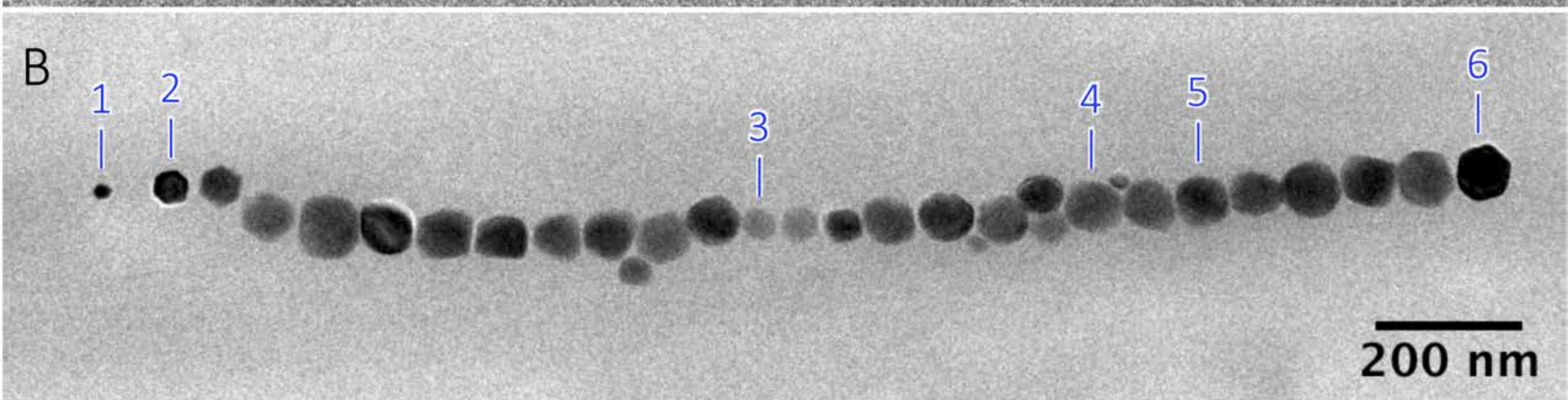
B
1
2
3
4
5
6
200 nm

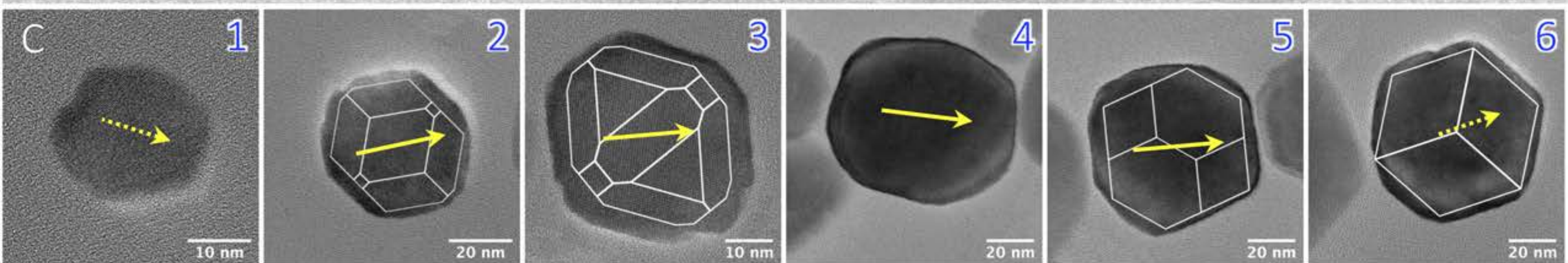
C
1
2
3
4
5
6
10 nm
20 nm
10 nm
20 nm
20 nm
20 nm

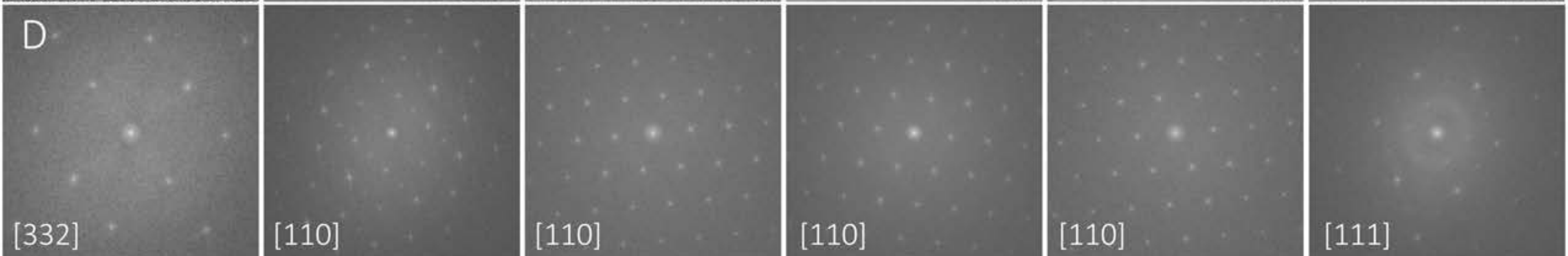
D
[332]
[110]
[110]
[110]
[110]
[111]

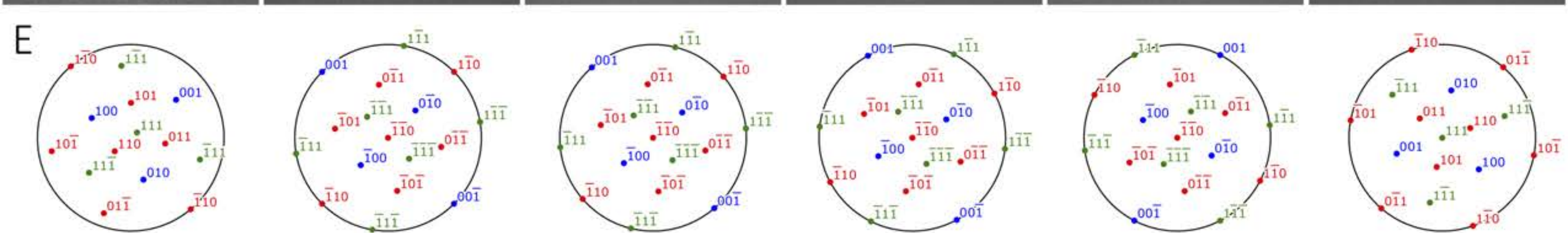
E